

# Automatic estimation of annual ring profiles in Norway spruce timber boards using optical scanning and deep learning



Osama Abdeljaber <sup>\*</sup>, Tadios Habite, Anders Olsson

Linnaeus University, Department of Building Technology, Sweden

## ARTICLE INFO

### Article history:

Received 4 May 2022

Accepted 2 October 2022

Available online 21 October 2022

## ABSTRACT

In softwood species, annual ring width correlates with various timber characteristics, including the density and modulus of elasticity along with bending and tensile strengths. Knowledge of annual ring profiles may contribute to more accurate machine strength grading of sawn timber. This paper proposes a fast and accurate method for automatic estimation of ring profiles along timber boards on the basis of optical scanning. The method utilizes two 1D convolutional neural networks to determine the pith location and detect the surface annual rings at multiple cross-sections along the scanned board. The automatically extracted rings and pith information can then be used to estimate the annual ring profile at each cross-section. The proposed method was validated on a large number of board cross-sections for which the pith locations and radial ring width profiles had been determined manually. The paper also investigates the potential of using the automatically estimated average ring width as an indicating property in machine strength grading of sawn timber. The results indicated that combining the automatically estimated ring width with other prediction variables can improve the accuracy of bending and tensile strength predictions, especially when the grading is based only on information extracted from optical and laser scanning data.

© 2022 The Author(s). Published by Elsevier Ltd. This is an open access article under the CC BY license (<http://creativecommons.org/licenses/by/4.0/>).

## 1. Introduction

Nondestructive evaluation of timber properties such as strength and stiffness is vital for the sawmilling industry. Accurate strength grading of timber boards leads to more effective utilization of material. The strength grading process is carried out either by visual inspection (i.e., visual strength grading) or using certified machines (i.e., machine strength grading) in order to classify boards into certain strength classes. The grading machines are used to determine certain indicating properties (IPs) that are strongly correlated with one or more of the three grade determining properties, namely bending or tensile strength, modulus of elasticity (MoE), and density [1].

In softwood species such as Norway spruce, there is in general a negative correlation between the annual ring width and both density and stiffness of clear wood (i.e. knot-free wood) [2]. Therefore, the European standards for visual strength grading of softwood, such as the British standard BS 4978 [3], the Nordic standard INSTA 142 [4], and the German standard DIN 4074–1 [5] impose certain upper limits on the average annual ring width. For example, the German standard classifies timber into three grading classes: S7,

S10, and S13, arranged from lowest to highest. The standard states that the maximum allowed average ring width is 4 mm for timber in class S13 and 6 mm for class S7 and S10 [5].

Multiple studies investigated the correlation between the average ring width and various wood characteristics, including the density and MoE along with bending, tensile, and compressive strengths [6,7]. Regarding the correlation with density, previous studies conducted on Norway spruce timber [8–10] reported various coefficients of determination  $R^2$  ranging from 0.18 to 0.38. Slightly stronger correlations have been reported between the annual ring width and bending strength [8,10–12] with  $R^2$  between 0.21 and 0.44. The coefficients of determination reported concerning the tensile strength are approximately on the same level (0.33 in [13] and 0.36 in [8]).

Currently, the annual ring width does not appear to be used as an IP (or involved in the definition of any IP) in the machine strength grading industry. Instead, the current grading machines rely on IPs based on properties that are easier to measure and have stronger correlations with the grade determining properties. The most commonly used IP for predicting the edgewise bending strength of timber is the longitudinal dynamic MoE. This IP can be determined quickly and inexpensively based on the timber board's density (determined as mass divided by volume or using X-ray) and length along with its first axial resonance frequency

\* Corresponding author.

E-mail addresses: [osama.abdeljaber@lnu.se](mailto:osama.abdeljaber@lnu.se) (O. Abdeljaber), [tadios.sisayhabite@lnu.se](mailto:tadios.sisayhabite@lnu.se) (T. Habite), [anders.olsson@lnu.se](mailto:anders.olsson@lnu.se) (A. Olsson).

determined by vibration testing. However, the  $R^2$  between the longitudinal dynamic MoE and Norway spruce's bending and tensile strength is only about 0.5 [14]. The reason is that the bending strength in timber is highly dependent on local weakening related to the presence of knots and related fiber directions, which cannot be captured very well by a global IP such as axial dynamic MoE [1]. Therefore, the axial dynamic MoE is often used in conjunction with high-resolution scanners that provide additional information regarding the local variations of material parameters. The most accurate grading machines currently in use combine axial dynamic testing with X-ray scanning [15]. However, an even more accurate method and procedure have been developed and verified, and approved settings for grading of timber in C-classes (EN 338:2016 [16]) are available [14]. This method is based on data of local fiber orientation obtained from laser scanning of board surfaces and it provides insights into how stiffness and strength vary along a board. In combination with knowledge of dynamic MoE, an IP was defined, which gives  $R^2$  in both bending and tensile strength as high as 0.69 and 0.66 (0.70 using non-linear regression), respectively, for large samples of Norway spruce timber [14,17].

Researchers have observed that combining the average ring width with other prediction variables results in a significantly more accurate strength prediction than when the average ring width is used on its own. Previous studies have shown that the  $R^2$  can be increased from 0.21 to 0.37 [8], 0.27 to 0.42 [11], and 0.20 to 0.39 [10] when the average ring width is combined with knot measurements in the prediction of bending strength of Norway spruce. Similar improvements were also achieved with regards to tensile strength (0.36 to 0.49 [8]). This shows that the annual ring width can be useful, in combination with other predictor variables, in definitions of IPs for machine strength grading.

Nonetheless, it remains a challenge to automatically and accurately detect the annual rings and measure the ring widths of timber under the conditions and speed of sawmill production. Most of the currently available methods for estimating the radial ring width profiles of timber boards and logs rely on computed tomography (CT) scanning [18–22]. Such methods involve applying Hough transform (HT) to detect the annual rings in cross-sectional CT images assuming that the rings are circular and concentric around the pith. The accuracy of these methods is very good; however, the high cost of operating a CT scanner is a significant issue when it comes to real applications. Thus, it would be of practical value if the less expensive optical scanners could be used to automatically detect the annual rings and estimate the rings widths.

In a recent study, Habite et al. [23] developed a method for locating the pith and estimate the radial profile of Norway spruce boards on the basis of surface scans obtained by a commercial optical scanner. The method applies a continuous wavelet transform (CWT) on the scanned surface images to estimate the distances between the surface annual rings on the four sides of a board. Simplex optimization was then used to obtain a radial profile that optimally fits the surface annual ring patterns estimated by the CWT. The method was verified over 104 Norway spruce boards, and the median error in the estimated pith location was around 5 mm.

However, the method proposed by Habite et al. [23] has three limitations. First, to reduce the parameters of the optimization problem, the method assumes a constant distance between consecutive rings (i.e., all rings have the same width), which is clearly unrealistic. Second, the simplex optimization requires around 180 ms on average to determine the radial profile of a single cross-section only, which is too slow considering the typical industry speed requirements (i.e., less than one second per board). Third, the ultimate purpose of that method was to locate the pith, and therefore the verification was limited to checking

the pith detection accuracy without verifying the detected rings or ring widths.

To address these limitations, the aim of the work presented in this paper is to utilize deep learning (DL) to develop a fast and accurate method for detecting annual rings and estimating the radial ring profiles along timber boards on the basis of optical surface scanning. The paper also includes an extensive evaluation of the potential of including information of annual ring widths, automatically extracted using the proposed method, in the definition of an IP for machine strength grading. The detailed objectives of this work are the following:

1. Train a DL model to detect surface rings on timber board surfaces scanned using an optical scanner.
2. Develop a method to estimate radial ring width profiles in clear wood based on the automatically detected pith locations and annual ring patterns detected on board surface.
3. Validate the proposed method on a large number of board cross sections for which pith locations and radial ring width profiles are determined manually.
4. Investigate the correlation between the automatically estimated average ring width and density.
5. Investigate the correlation between average ring width (when used as an IP in itself or in combination with other prediction variables) and *tensile strength* of a large sample of destructively tested Norway spruce boards.
6. Conduct the corresponding statistical analysis regarding the correlations with *bending strength* for another large sample of destructively tested Norway spruce boards.

## 2. Material, collected data and definitions of properties

### 2.1. Material and data from scanners

Altogether, four sets of boards were investigated in this research, two for comparison between automatically and manually estimated average ring width over cross sections, and two for investigation of correlations between average ring width and other board properties. All boards included were of Norway spruce, planned on four sides and approximately of dimension  $45 \times 147 \text{ mm}^2$ .

#### 2.1.1. Board set one – Five boards scanned with CT scanner and optical scanner

Board set one consists of five boards of length 3.6 m, originating from southern Sweden. These boards were scanned using an X-ray CT scanner [22]. The resolution obtained data was 0.3 mm per pixel in the three directions. From this data, 20 images of board cross sections were extracted from each board (approximately 18 cm between extracted sections). Fig. 2a shows an image of a board cross section obtained from X-ray CT scanning.

The five boards were also scanned using an industry optical laser scanner such that red, green, and blue (RGB) images as well in-plane fiber direction, the latter obtained using laser and the tracheid effect [24–26], were obtained for each of the four longitudinal board surfaces with resolution of about  $0.8 \times 0.07 \text{ mm}^2$  and  $4.4 \times 1.0 \text{ mm}^2$  (lengthwise  $\times$  crosswise board direction), respectively. Fig. 1c-d show an RGB image and an image of in-plane fiber direction, respectively, for a part of a longitudinal board surface.

#### 2.1.2. Board set two – 76 boards scanned with two different optical scanners

Board set two consists of 76 boards of length 5.100 mm, originating from the area around Notnäs in South-mid Sweden. For these boards, both end cross sections were scanned using a common optical flatbed scanner to obtain images as the one shown



**Fig. 1.** Images obtained from scanning; (a) image of a board cross section obtained from X-ray CT scanning, (b) image of an end cross section obtained using a flatbed scanner, (c) RGB image of a longitudinal board surfaces and (d) in-plane fiber orientation of a longitudinal board surface. (c and d obtained using an industry optical laser scanner.).

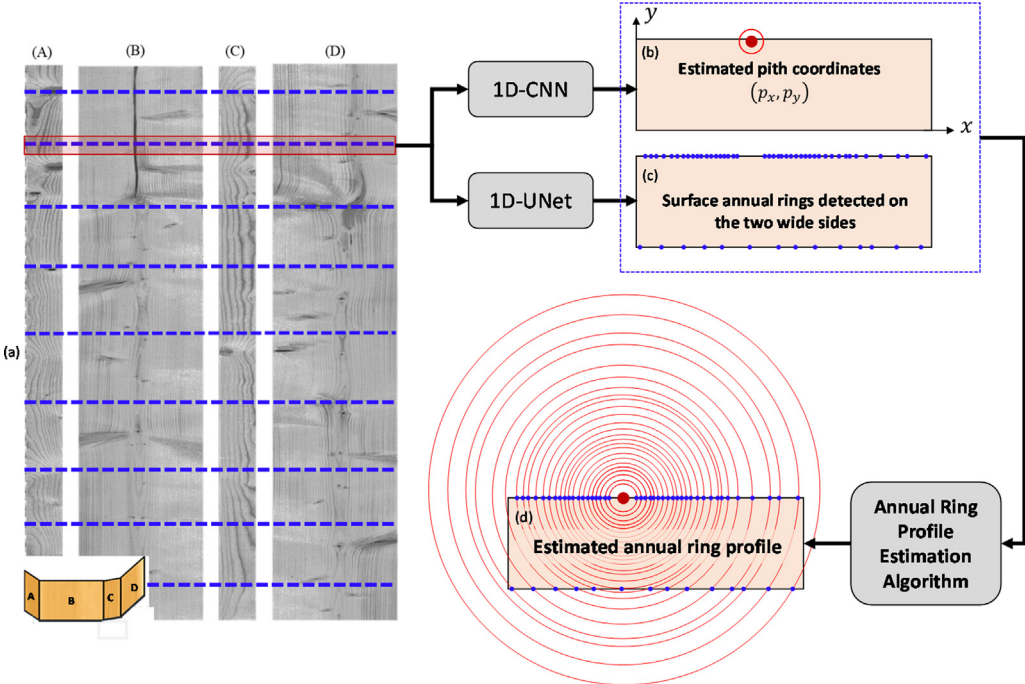


**Fig. 2.** Overview of the proposed method for automatic estimation of annual ring profiles: (a) Grayscale images of the four sides of the board are obtained, and  $N$  locations along the board are considered. (b) At each cross-section, the 1D-CNN identifies the pith location. (c) At each cross-section, the 1D-UNet detects the surface rings on the two wide faces. (d) The estimated pith location and surface rings are used to estimate the annual ring profiles at the  $N$  cross-sections.

in Fig. 1b. The boards were also scanned using the same industry optical laser scanner as used for board set one, to obtain images of lateral surfaces as those shown in Fig. 1c-d.

#### 2.1.3. Board set three – 383 boards scanned and destructively tested in tension

Board set three consists of 383 boards of various lengths obtained from six different sawmills located in different parts of Sweden and Finland. The boards in set three are a subsample of a larger sample of more than 900 boards used for a comprehensive investigation on the performance of the above-mentioned machine strength grading method (utilizing local fiber direction in combination with dynamic MoE) [17] for prediction of tensile strength and grading of boards into  $T$ -classes. The current board set three consists of the boards of dimension  $45 \times 145 \text{ mm}^2$  of the sample of boards presented in [17]. Relevant collected data for the boards comprise the following: RGB images and data of in-plane fiber orientation on four sides of the boards obtained from the industry optical scanner, dimensions, weight, longitudinal resonance frequency, clear wood density, moisture content, and stiffness and strength properties obtained from tensile tests, as developed in the subsequent Section 2.1.4.

#### 2.1.4. Board set four – 409 boards scanned and destructively tested in bending

Board set four consists of 409 boards of various lengths obtained from seven different sawmills in different parts of Sweden, Norway and Finland. In [14], an investigation comprising more than 900 boards of various dimensions was performed to evaluate the same machine strength grading method as in [17] but for prediction of bending strength, rather than tensile strength. The boards in the current set four consists of the boards of dimension  $45 \times 145 \text{ mm}^2$  of the investigation reported in [14]. Relevant collected data is the same as for board set three, except that stiffness and strength properties were obtained from four point bending tests, as developed in the subsequent Section 2.1.4, rather than from tensile tests. Board set two (see Section 2.1.2) was actually a subset of board set four.

#### 2.2. Definitions of predictor variables and grade determining properties

The data collected for board sets three and four (boards tested destructively in bending and tension, respectively) give basis for calculation of a number of prediction variables and grade deter-

mining properties (GDPS). The prediction variables constitute, or give basis for, IPs for prediction of GDPS, in particular bending and tensile strength.

For boards of set 3–4, the board mass  $m$ , length  $L$ , depth  $h$  and thickness  $t$ , and the board moisture content  $u_s$ , were determined manually. A scale was used for weighing, and a pin-type moisture meter was used to determine the moisture content. The lowest longitudinal resonance frequency of the boards,  $f_1$ , were determined manually in laboratory using impact hammer, an accelerometer and a vibration analyzer utilizing fast Fourier transform (FFT). In the investigations presented in [14] and [17], dimensions, mass/density and resonance frequency were also determined using strength grading machines, but the data utilized herein is from manual measurements.

Board density adjusted to 12 % moisture content was calculated as,

$$\rho_{\text{board},12\%} = \frac{m}{L \cdot h \cdot t} \left( 1 - \frac{u_s - 12}{200} \right) \quad (1)$$

After destructive tests, clear wood specimens were cut from the boards and the clear wood density adjusted to 12 % moisture content,  $\rho_{\text{cw},12\%}$ , were determined according to instructions EN 408:2010 [27]. ( $\rho_{\text{cw},12\%}$  is identical to the grade determining density,  $\rho$ , defined in EN 384:2016 [28].).

The axial dynamic MoE, adjusted to 12 % moisture content, was calculated as,

$$E_{\text{dyn},12\%} = 4 \frac{m}{L \cdot h \cdot t} f_1^2 L^2 \left( 1 + \frac{u_s - 12}{100} \right) \quad (2)$$

where the moisture content adjustment factor  $(1 + (u_s - 12)/100)$  is derived from EN 384 [28]. A prediction variable, similar to  $E_{\text{dyn},12\%}$ , although not based on knowledge of density, was defined as,

$$D_{\text{dyn},12\%} = f_1^2 L^2 \left( 1 + \frac{u_s - 12}{100} \right) \quad (3)$$

Another prediction variable evaluated herein is based on knowledge of local fiber orientation (see Fig. 1d) of all four longitudinal sides of a board. By assuming values representative for Norway spruce wood for modulus of elasticity in fiber direction and perpendicular directions, shear moduli and poisson's ratios, local MoE in the board's longitudinal direction was calculated. Then, by integrating this local MoE over cross sections along the board, a bending stiffness profile along was established (moving average of calculated bending stiffness over 90 mm along the board applied) and the minimum value along the profile, denoted  $E_{\text{b},90,\text{nom}}$ , was considered a prediction variable to strength. For a thorough description and definition of this indicating property, and how it in previous works has been utilized in definitions of IPs to bending and tensile strength, see [1] and [17], respectively.

Four point bending tests and tensile tests were performed according to EN 408 [27] for board sets three and four, respectively. Based on these tests bending strength,  $f_m$ , and tensile strength,  $f_t = f_{t,0}$  were determined for boards of set three and four, respectively. Characteristic values of these strengths are GDPS, see EN 384 [28].

### 3. Method

Fig. 2 presents an overview of the proposed method. The method utilizes the four RGB images obtained by scanning the four surfaces of a board using an industrial optical scanner. The red and blue channels of the images are discarded, and the green channel is used to obtain grayscale images. The first step is to identify the pith locations at  $N$  cross-sections along the board using a pith detection

technique recently developed by the authors [29], which utilizes one-dimensional convolutional neural networks (1D-CNNs). Then, at each evaluated cross-section, a 1D-UNet is used to detect the surface rings on the two wide surfaces. After that, a simple algorithm is applied to identify the annual ring profile at the  $N$  cross-sections based on the automatically estimated pith location and surface rings.

This section describes each step of the proposed method, including a summary of the pith detection technique presented in [29], a detailed description of the training and application of the 1D-UNet used for detecting surface rings, and finally the ring profile estimation algorithm. A brief background on 1D-CNNs and 1D-UNets is provided in the next subsection since these DL models are central to this work.

#### 3.1. 1D-CNNs

CNNs are DL models suitable for computer vision tasks such as image classification and object detection. 1D-CNNs are a special case of CNNs designed to operate over 1D signals instead of 2D images. They have been successfully used in challenging signal classification and regression tasks such as detection of anomalies in electrocardiogram (ECG) signals [30] and damage identification in machines and structures [31,32].

As shown in Fig. 3, a typical 1D CNN begins with alternating 1D convolution and pooling layers for extracting features from the input signals, followed by multilayer perceptron (MLP) layers used to compute the final output as a nonlinear function of the extracted features. For a 1D convolution layer,  $l$ , having  $N_f$  kernels,  $M$  input channels and  $S$  samples in each channel, the  $j^{\text{th}}$  output feature vector of this layer is [33]:

$$\mathbf{y}^{j,l} = \left[ y_i^{j,l} \right] = f(b_j^{j,l} + \mathbf{x}^{j,l}) \quad (4)$$

where,

$$\mathbf{x}^{j,l} = \left[ x_i^{j,l} \right] = \mathbf{Y}^{l-1} * \mathbf{W}^{j,l} \quad (5)$$

$$\mathbf{x}^{j,l} = \sum_{r=1}^K \sum_{c=1}^M y_{[i+r-1,c]}^{l-1} W_{[r,c]}^{j,l} \quad (6)$$

where the operator  $(*)$  denotes a standard 1D convolution operation with a single stride and no zero padding,  $K$  is the filter size,  $\mathbf{Y}^{l-1}$  is a matrix of size  $S \times M$  that contains the output feature vectors of the previous layer,  $l-1$ ,  $\mathbf{W}^{j,l}$  is the  $j^{\text{th}}$  filter (a matrix of size  $K \times M$ ) of the current convolution layer,  $l$ ,  $b_j^{j,l}$  is a scalar bias, and  $f(\cdot)$  is an activation function. The index  $i$  ( $1 \leq i \leq S - K + 1$ ) denotes a sample in the vectors  $\mathbf{y}^{j,l}$  and  $\mathbf{x}^{j,l}$ .

Each 1D convolution layer is usually followed by a 1D pooling layer that downsamples the feature vectors  $\mathbf{y}^{j,l}$ . Through consecutive convolution and pooling operations, 1D CNNs extract high-level features from the input signals, which are then combined into a single vector (i.e., flattened) and fed into the MLP layers. For a MLP layer,  $l$ , with  $N$  neurons and  $P$  inputs, the output  $\mathbf{y}^l$  (vector of size  $N$ ) can be written as:

$$\mathbf{y}^l = g(\mathbf{b}^l + \mathbf{W}^l \mathbf{y}^{l-1}) \quad (7)$$

where  $\mathbf{b}^l$  is a bias vector of size  $N$ ,  $\mathbf{W}^l$  is a weighting matrix of size  $N \times P$ ,  $\mathbf{y}^{l-1}$  is the output of the previous layer  $l-1$  (a vector of size  $P$ ) and  $g(\cdot)$  is an activation function.

##### 3.1.1. 1D-UNet

The UNet is a CNN architecture commonly used in semantic segmentation [34] and image-to-image translation [35]. Unlike the conventional CNN architecture described above, which is usu-

ally used to produce a very limited number of outputs, UNets are capable of generating high-resolution outputs, typically having the same resolution as the input image.

The 1D-UNet is a one-dimensional version of the UNet architecture suitable for signal denoising [36] and signal-to-signal translation [37]. It consists of a contracting part (i.e., the encoder) followed by an expansive part (i.e., the decoder). As illustrated in

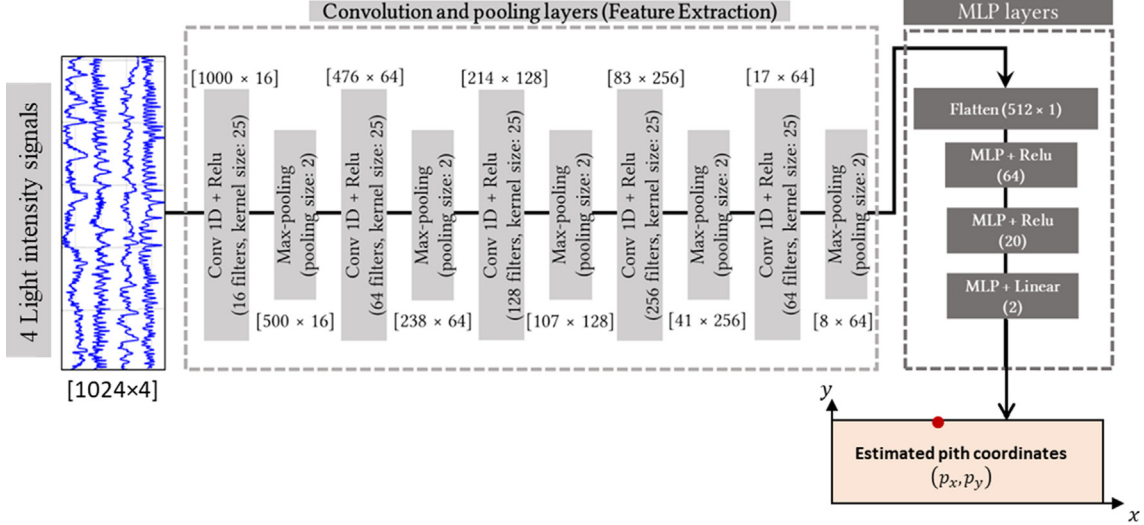


**Fig. 3.** The architecture of the 1D CNN used to locate the pith [29]. The rectified linear unit (Relu) activation function is used for all convolution and MLP layers except the last MLP layer which has linear activation. The quantities between the square brackets correspond to the number of samples  $\times$  the number of output feature vectors of each convolution and pooling layer.

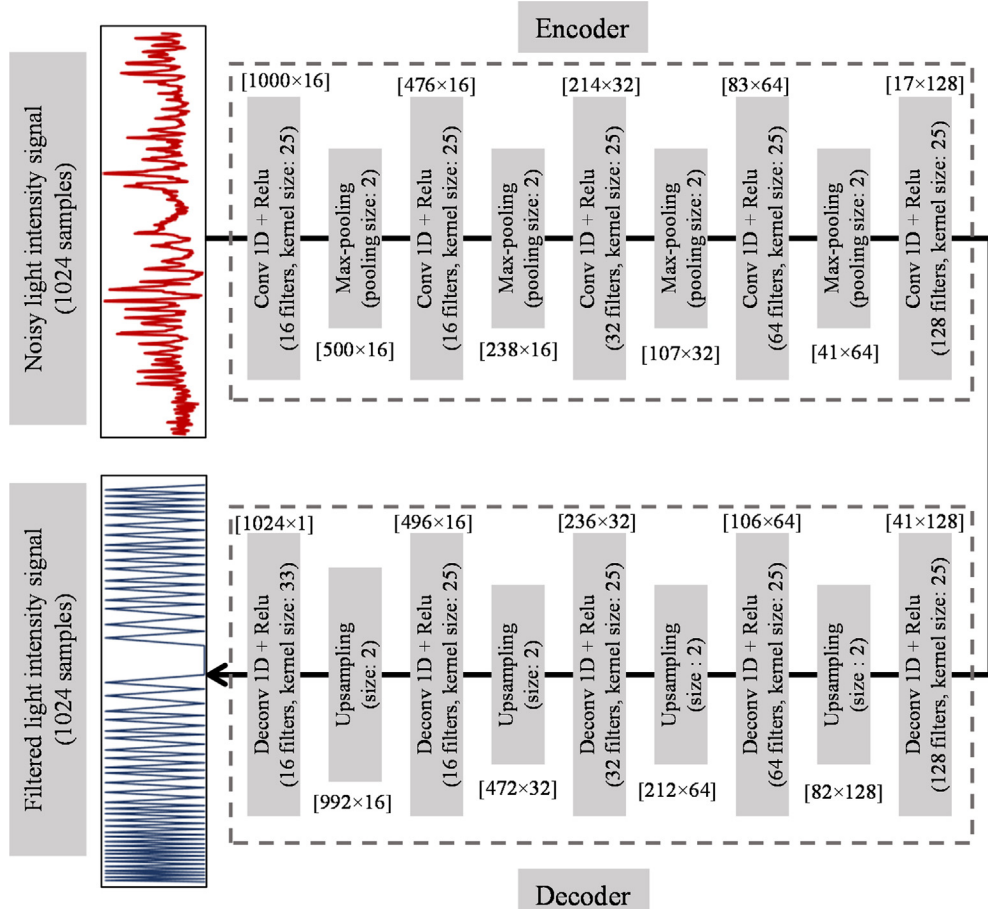


**Fig. 4.** The architecture of the 1D UNet used to detect surface rings. The rectified linear unit (Relu) activation function is used for all convolution deconvolution layers. The quantities between the square brackets correspond to the number of samples  $\times$  the number of output feature vectors of each convolution and pooling layer.

**Fig. 4**, the encoder is built up of alternating 1D convolutional and downsampling layers, while the decoder consists of consecutive 1D deconvolution and upsampling layers. The convolution and pooling layers of the encoder extract low-resolution features from the input signals. These features are then processed and gradually upsampled through the decoder's layers until a full-resolution output signal emerges from the last layer.

The 1D convolution operations that take place in the encoder are described by Eq. 4–7. Regarding the decoder, the output  $\mathbf{x}^{j,l} = [x_i^{j,l}]$  of a standard 1D deconvolution operation (i.e., deconvolution with a single stride and no zero padding) between the output features of the previous layer  $\mathbf{Y}^{l-1}$  and the  $j^{\text{th}}$  filter of the current deconvolution layer  $\mathbf{W}^{j,l}$  can be written as:

$$\mathbf{x}^{j,l} = \sum_{r=\max(1,i-S+1)}^{\min(K,i)} \sum_{c=1}^M y_{[i-r+1,c]}^{l-1} w_{[r,c]}^{j,l} \quad (8)$$

The  $j^{\text{th}}$  output feature vector of a 1D deconvolution layer,  $l$ , with  $N_f$  kernels after adding the bias  $b^{j,l}$  and applying the activation function is given as:

$$\mathbf{y}^{j,l} = [y_i^{j,l}] = f(b^{j,l} + \mathbf{x}^{j,l}) \quad (9)$$

where the index  $i$  ( $1 \leq i \leq S + K - 1$ ) denotes a sample in the vectors  $\mathbf{y}^{j,l}$  and  $\mathbf{x}^{j,l}$ .

### 3.1.2. Training of 1D-CNNs

Both conventional 1D CNNs and 1D-UNets are supervised neural networks, which means they should be trained over a dataset consisting of a large number of input signals along with the corresponding desired targets. The training of a 1D-CNN starts by randomly initializing its parameters (i.e., the weighting filters of the convolution and deconvolution layers and the weights of the MLP layers). An iterative optimization process is then carried out to optimize these parameters. This process involves two operations, forward- and back-propagation. In forward-propagation, an input signal is propagated from the first layer up until the last one according to Eqs. (1)–(5) above. The output that emerges from the output layer is compared to the desired target corresponding to that input signal using a certain loss function such as mean squared error (MSE) and mean absolute error (MAE). The calculated error is then back-propagated through the CNN starting from the last MLP layer up until the first convolution layer. During the back-propagation process, the sensitivity of each parameter in the 1D-CNN to the error is computed. The sensitivities are then used to iteratively update the 1D CNN parameters until a certain stop criterion is met. Gradient-descent (GD) algorithms, such as Adaptive Moment Estimation (Adam) [38], can be used in the training process.

### 3.2. Estimation of pith locations

As mentioned earlier, the first step in the proposed radial profile estimation method is to predict the pith location at  $N$  cross-sections along a board using the pith detection technique presented in [29]. This technique is based on a well-trained 1D-CNN that estimates the x- and y-coordinates of the pith location at each evaluated cross-section given the light intensity variations across the four sides of the board. Four light intensity signals are obtained at each cross-section by taking a single pixel line (represented in **Fig. 1** by dashed blue lines) from the four grayscale images. The four signals are normalized between 0 and 1, resampled to 1024 samples, and then fed into the 1D-CNN to estimate the pith location at the cross-section. The 1D-CNN has the standard architecture shown in **Fig. 3**, which consists of five convolution/pooling blocks followed by three MLP layers.

### 3.2.1. Training of the pith estimator

To train the pith estimator, it is necessary to have a large training dataset consisting of thousands of light intensity signals (i.e., inputs) together with the corresponding actual pith locations (i.e., targets). Obtaining this kind of dataset for real boards would require scanning of hundreds of boards, dissecting them at several locations, and then estimating the pith location of each cross-section manually. In order to avoid this laborious and time-consuming exercise, a virtual board generator, recently developed by the authors [29], was used to generate the training dataset. The board generator consists of two components: a stochastic log model and a conditional generative adversarial neural network (cGAN). The stochastic log model is used to generate a random 3D log (knots not included) with realistic annual rings. Binary board surfaces are then obtained by cutting a board at a random location within the 3D log. The binary images (where the zeros represent annual rings and the ones represent the background) are then processed by the cGAN, which transforms them into photorealistic images of Norway spruce surfaces. The overall process is illustrated in **Fig. 5**. The interested reader is referred to [29] for more details on the stochastic log model as well as the cGAN.

The virtual board generator was used to generate 3000  $145 \times 45 \times 205\text{-mm}^3$  boards with photorealistic surfaces and known pith locations and radial profiles. A total of 120,000 input-target training samples were collected by obtaining the light intensity signals and the corresponding pith locations at 40 locations along each board. 80 % of the training samples were used for training while the remaining 20 % were kept for validation. Further details about the training of the pith detector can be found in [29].

### 3.3. Detection of surface rings

**Fig. 6** shows examples of light intensity signals obtained from images of Norway spruce timber surfaces obtained from scanning. It is clear that the local minima of a light intensity signal coincide with the latewood part of the annual rings at that location. However, it can also be noticed that these signals are contaminated by noise and other artifacts, making it difficult for conventional peak-finding algorithms to differentiate between the local minima that correspond to the rings and those arising from the noise. Therefor a 1D-UNet was trained to denoise the light intensity signals so that the surface rings can be easily identified. The idea is to train the 1D-UNET to translate the input light intensity signal into a corresponding output signal with triangular spikes (**Fig. 4**). The tips of the spikes represent the actual locations of the surface rings at the location where the light intensity signal was taken. All spikes have the same amplitude of 1.0. The slope of each spike is inversely proportional to the distance to the neighboring rings. In other words, closely spaced rings are represented by triangular spikes with large slopes while sparsely spaced rings are represented by spikes with small slopes.

The architecture of the encoder and decoder of the 1D-UNet is given in **Fig. 4**. The encoder takes a single light intensity signal with a resolution of 1024 samples and applies successive convolution and subsampling operations to extract 128 low resolution features (17 samples). The decoder applies consecutive deconvolution and upsampling operations on the extracted features until a single output signal with the same resolution as the input (1024 samples) emerges from the last layer.

The 3000 photorealistic virtual boards described in **Section 3.2.1** were also utilized to train the 1D-UNet. From each board, the light intensity signals on the two wide sides were collected at 40 evenly spaced locations. The surface ring locations on the two wide sides were acquired at the same locations. The ring information extracted from the boards were used to generate target signals

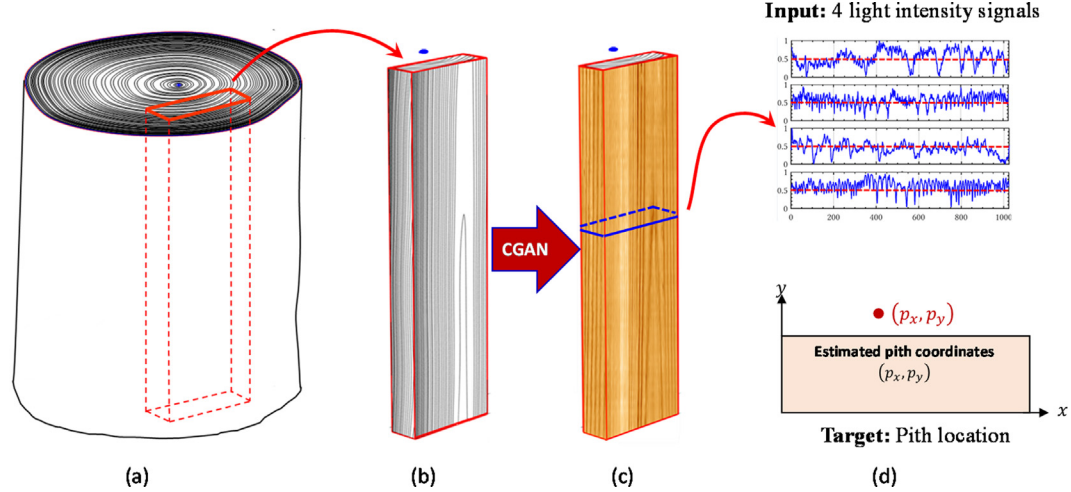


**Fig. 5.** Summary of the training data generation process. (a) The stochastic log model is used to generate a random log. (b) Binary board surfaces are obtained by cutting a board at a random location within the 3D log. (c) A cGAN model is used to translate the binary images into photorealistic images of Norway spruce surfaces. (d) The photorealistic boards are used to generate input-target pairs required for training the pith detector.

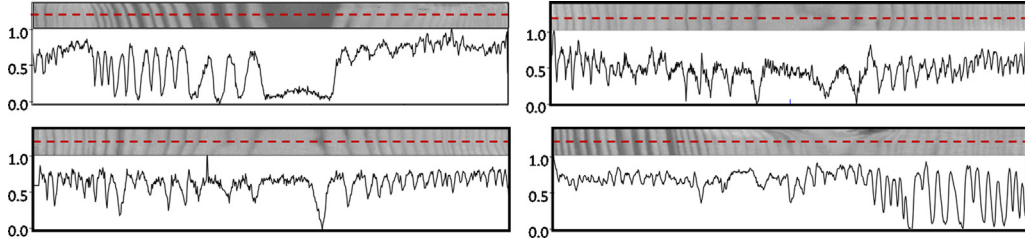


**Fig. 6.** Examples of noisy light intensity signals from Norway spruce surfaces.

with triangular spikes that represent the surface rings. This process resulted in a total of 240,000 input-target pairs (i.e., 3000 boards  $\times$  2 wide sides  $\times$  40 locations).

Out of the 240,000 training samples, 80 % were used for training and 20 % for validation. MAE was used as a loss function in the training process. The training was carried out in Tensorflow 2.0 [39] using Adam optimizer with a learning rate of 0.001 and a batch size of 128. During the training, 1D-CNN's performance over the validation set was monitored in terms of the MAE. The training process was terminated after 29 epochs when the performance over the validation set stopped improving in order to prevent overfitting.

### 3.3.1. Post-processing of 1D-UNet outputs

After training the 1D-UNet, it was preliminarily tested over a few light intensity signals extracted from real Norway spruce surfaces. We noticed that the UNet was generally successful in denoising the input light intensity signals and producing an output signal with distinctive peaks. However, the tests also revealed that further post-processing of the output signals is required for extracting the ring locations.

As an example, Fig. 7b shows a noisy light intensity signal taken from a real Norway spruce surface (Fig. 7a). Ideally, the UNet would produce a corresponding output signal like the one in Fig. 7c, where the ring locations could be directly identified as the tips of the spikes (i.e., the "ones" in the signal). Nonetheless, the preliminary tests showed that the actual 1D-UNet output is similar to the signal in Fig. 7d, where the tips of the spikes do not necessarily go all the way up to 1.0, and the parts of the signal between the spikes do not always go all the way down to 0.0. This means that the rings cannot simply be found in a filtered light

intensity signal by picking data points at a certain constant value. Fortunately, this issue can be easily addressed by the following post-processing steps:

1. Set all data points with values less than or equal to 0.5 to zero.
2. Set all data points above 0.5 to one.
3. The rings can be then identified as the centroids of the "ones" regions in the resulting binary signal (see Fig. 7e and f).

### 3.4. Automatic estimation of radial profiles

The next step, after identifying the pith location at a particular cross-section and detecting the surface rings on both wide surfaces, is to identify the radial profile of the cross-section (i.e., the radii of the annual rings). Consider a board cross-section having a width of  $W$  in the x-direction and a depth  $T$  in the y-direction with an estimated pith location of  $(p_x, p_y)$  and surface rings detected on both wide sides. As shown in Fig. 8, the *near side* is defined as the wide side closer to the estimated pith location in the y-direction, while the opposite side is called the *far side*. If the x-coordinate of the estimated pith location is within the width of the board ( $0 < p_x < W$ ), then both the far and near sides can be divided into short and long segments. The surface rings detected on both sides can then be divided into four groups (arranged from the most important to the least important):

1.  $G_1$ : Detections on the long segment of the far side.
2.  $G_2$ : Detections on the short segment of the far side.
3.  $G_3$ : Detections on the long segment of the near side.
4.  $G_4$ : Detections on the short segment of the near side.

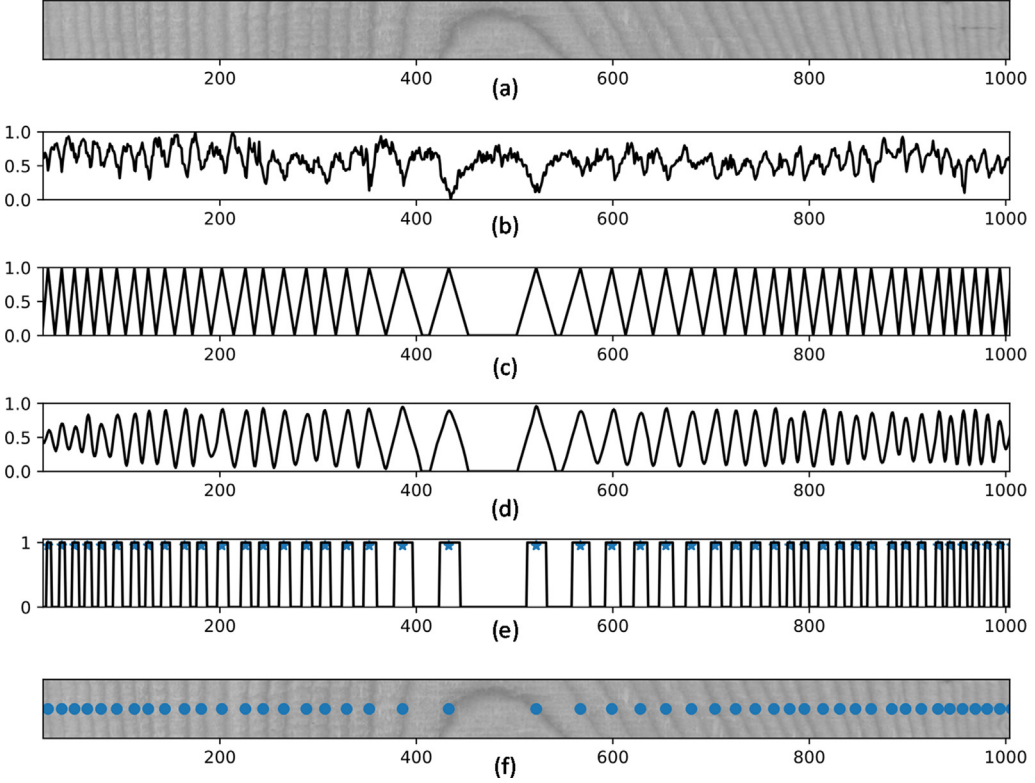


**Fig. 7.** Post-processing of 1D-UNet outputs. (a) Norway spruce surface image. (b) Original light intensity signal (i.e., the input). (c) Ideal filtered signal. (d) Actual filtered signal obtained by processing the input signal using the 1D-UNet. (e) Binary signal after obtaining by setting all values greater than 0.5 to 1.0, and all values  $\leq 0.5$  to 0.0. (f) The surface rings are identified as the centroids of the “ones” regions.

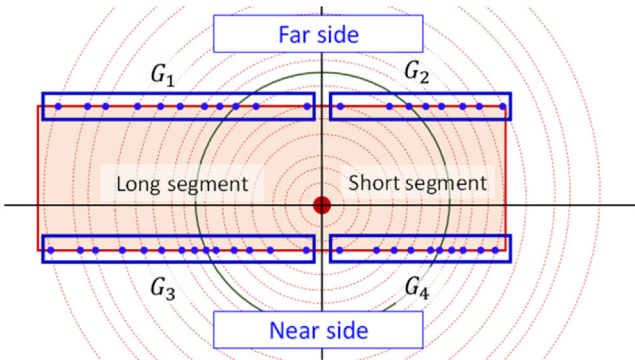


**Fig. 8.** Description of the algorithm used to estimate annual ring profiles on the basis of the detected pith and surface rings. The solid green ring is an example of a ring that intersects with both the far and near sides and with both short and long segments. (For interpretation of the references to colour in this figure legend, the reader is referred to the web version of this article.)

The detections on the far side are prioritized over the ones on the near side since we noticed that the surface rings are clearer and more distinctive on the face further away from the pith. The annual rings obviously intersect more with the long segments, and therefore the detections on the long segments are prioritized over the ones on the short segments.

The estimated radii of the annual rings  $r_{ij}$  corresponding to the detections in the  $i^{\text{th}}$  group can be calculated as:

$$r_{ij} = \sqrt{(p_x - x_{ij})^2 + (p_y - y_{ij})^2} \quad (10)$$

where  $x_{ij}$  and  $y_{ij}$  are the coordinates of the  $j^{\text{th}}$  detection in the  $i^{\text{th}}$  group.

It is very likely that an annual ring intersects with both the far and near sides and/or with both the long and short segments (see Fig. 8). Hence, the radii identified in the four groups are not unique. In other words, the same ring can simultaneously appear in two or more groups. The estimated radii corresponding to the same ring are most probably not equal since the annual surface rings are not perfectly circular, which makes it challenging to determine whether two similar radii belong to the same ring or to different rings.

In order to combine the radii from the four groups into a single radial profile with unique annual rings, we adopted the following approach:

1. The radii of the four groups are sorted in ascending order.
2. All radii in  $G_1$  are assumed to belong to unique rings. The set of unique rings is initially set to  $U = [r_{1,1}, r_{1,2}, \dots, r_{1,N_1}]$ , where  $N_1$  is the number of detections in  $G_1$ .
3. The radial distances between consecutive rings (i.e. ring widths) in  $G_1$  is calculated as:

$$d_{1,j} = r_{1,j+1} - r_{1,j} \quad (11)$$

4. A threshold  $h$  is defined as a parameter  $\alpha$  multiplied by the mean ring width in  $G_1$ ,  $\bar{d}_1$ :

$$h = \alpha \bar{d}_1 \quad (12)$$

As will be clarified in the next steps, this threshold is used when comparing the radii in the remaining three groups to the unique radii in the set  $U$  in order to decide whether to add them to  $U$  or discard them.

5. Each radius  $r_{2,j}$  in  $G_2$  is compared to all unique radii in  $U$ . If the minimum difference between  $r_{2,j}$  and the radii in  $U$  exceeds the threshold  $h$ , the radius  $r_{2,j}$  is added to the set  $U$ . Otherwise, the

radius is considered to be too similar to the current radii in  $U$ , and therefore discarded.

6. The process is repeated over all radii in  $G_3$  and then  $G_4$ . The radii that are sufficiently unique, as measured by the threshold  $h$ , are added to the set  $U$ .

The threshold  $h$  adapts to the ring density of the analyzed cross-section. In cross-sections with closely spaced rings, the mean ring width in  $G_1$ ,  $\bar{d}_1$ , will be small, resulting in a small  $h$ . On the other hand, boards with low ring density will have a large  $\bar{d}_1$  and therefore a large  $h$ . This means that in cross-sections with sparsely spaced rings, a new ring is added to  $U$  only if its radius is significantly different from the radii of the rings in  $U$ . In boards with high ring density, a new ring can be admitted to  $U$  even if it is very close to one of the rings in  $U$ .

In addition to the ring density, the value of  $h$  depends on the parameter  $\alpha$ . A systematic analysis of the effect of  $\alpha$  on the accuracy of the proposed radial estimation approach will be presented in Section 4. An appropriate  $\alpha$  value will be selected and adopted thereafter.

### 3.5. Manual estimation of radial profiles

To obtain the data required for validating the proposed method, the radial profiles were manually estimated at 20 locations along each of five CT-scanned boards as well as at the two end cross-sections of 76 Norway spruce boards. The manual labeling was done in a graphical user interface (GUI) developed specifically for this purpose. The labelers were instructed to start by carefully labeling at least three “main rings”. The labeling of a main ring is done by clicking several points on the ring. The interface then calculates the radius of the circle that best fits the clicked points in a least square sense. After labeling a sufficient number of main rings, the pith location is calculated as the mean of the rings’ centers. The labeler then proceeds to label the rest of the rings. Given the pith location estimated from the main rings, it is sufficient to click a single point on each of the remaining rings to calculate their radii. The process, which is illustrated in Fig. 9, can be performed on images of board cross sections obtained either from CT scanning or from optical scanning.

## 4. Results and discussion

A total of 252 Norway spruce cross-sections (board set 1–2) were used to validate the proposed method. The potential of using

the annual rings information in machine strength grading of Norway spruce was evaluated over a large sample consisting of 792 boards (board set 3–4). The results are reported and discussed in the following subsections.

### 4.1. Validation over CT-scanned boards

The method was initially validated over 100 cross-sections obtained from the five Norway spruce boards of board set one, scanned both by an optical and a CT scanner as described in Section 2.1.1. The radial profiles of the 100 cross-sections were manually identified as explained in Section 3.5.

The automatic radial profile estimation method was then carried out based on images of the four longitudinal sides of each board obtained from optical scanning. First, light intensity signals were obtained at every 20 pixels along each evaluated board (approximately 300 locations per board). Second, all signals were normalized between 0 and 1, resampled to 1024 samples, and then fed to the 1D-CNN in order to estimate the pith location at each location. Fig. 10a shows estimated pith locations along a board, represented by red lines drawn on top of images of wide and narrow side, respectively, along the board. Although the estimated pith locations look reasonable at knot-free regions, one can notice significant disturbances at the knotty areas. The reason is that the 1D-CNN was trained exclusively on clear wood surfaces and therefore did not learn how to handle knots. To reduce the significant disturbances related to knots, a moving mean filter was applied on the x- and y-coordinates of the estimated pith locations. The resulting, filtered pith location is shown in Fig. 10b.

Third, the 1D-UNet was used to denoise the light intensity signals of the two wide surfaces. The output signals were post-processed as described in Section 3.3.2 to identify the surface rings on the wide sides at the 300 locations. Fig. 11 shows examples of the performance of the surface ring detector. Similar to the pith estimator, the annual ring detector works very well on clear wood areas, but it does not provide reliable detection in areas with knots. This is due to the fact that the 1D-UNet was train only on knot-free virtual wood surfaces.

Fourth, the algorithm presented in Section 3.4 was applied to estimate the corresponding radial profiles given the filtered pith locations and the detected surface rings. Finally, the automatically estimated ring profiles were compared to their manually estimated counterparts at the 20 evenly spaced cross-sections along each board in terms of both the number of detected rings and the aver-

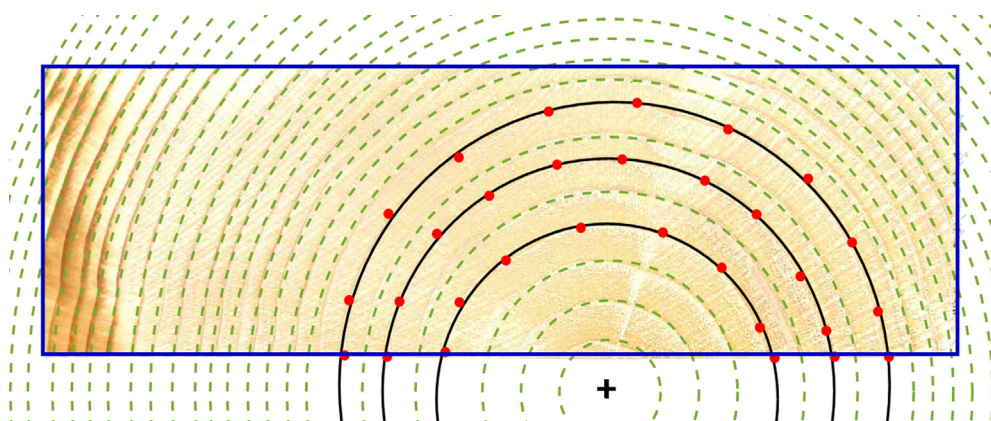


**Fig. 9.** Manual estimation of annual ring profiles using the GUI: 1- The labeler starts by clicking multiple points (red dots) on at least three “main rings”. The radii and centers of the circles that best fit the clicked points are calculated (solid black circles). The pith location is estimated as the average of the main rings’ centers. The remaining rings (dashed green circles) are then labeled by clicking a single point per ring (given the estimated pith location). (For interpretation of the references to colour in this figure legend, the reader is referred to the web version of this article.)

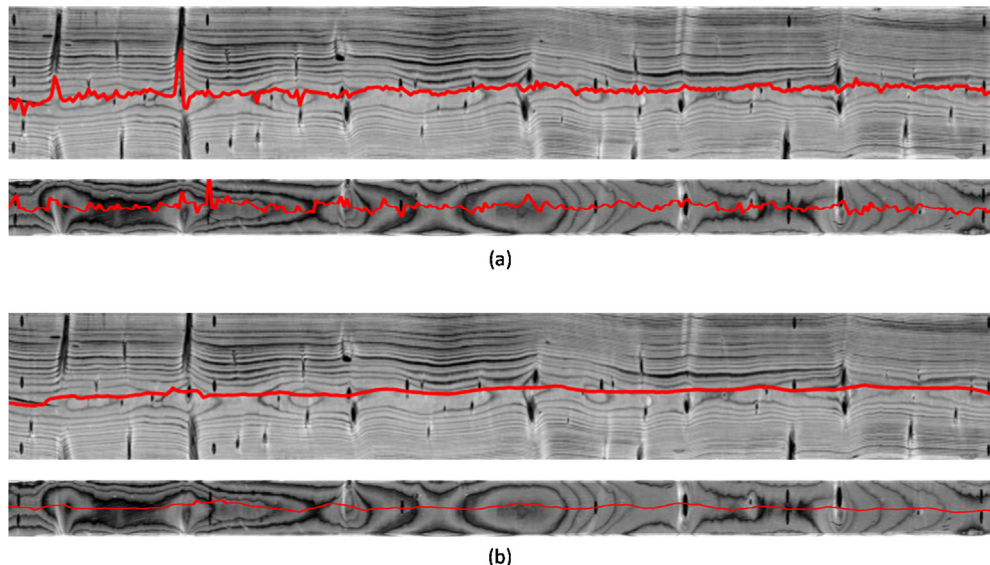


**Fig. 10.** Pith locations on the wide and narrow sides of a Norway spruce board identified by the 1D-CNN: (a) before applying the moving average filter, and (b) after applying the moving average filter with a window size of 10 data points (approximately 10 cm).

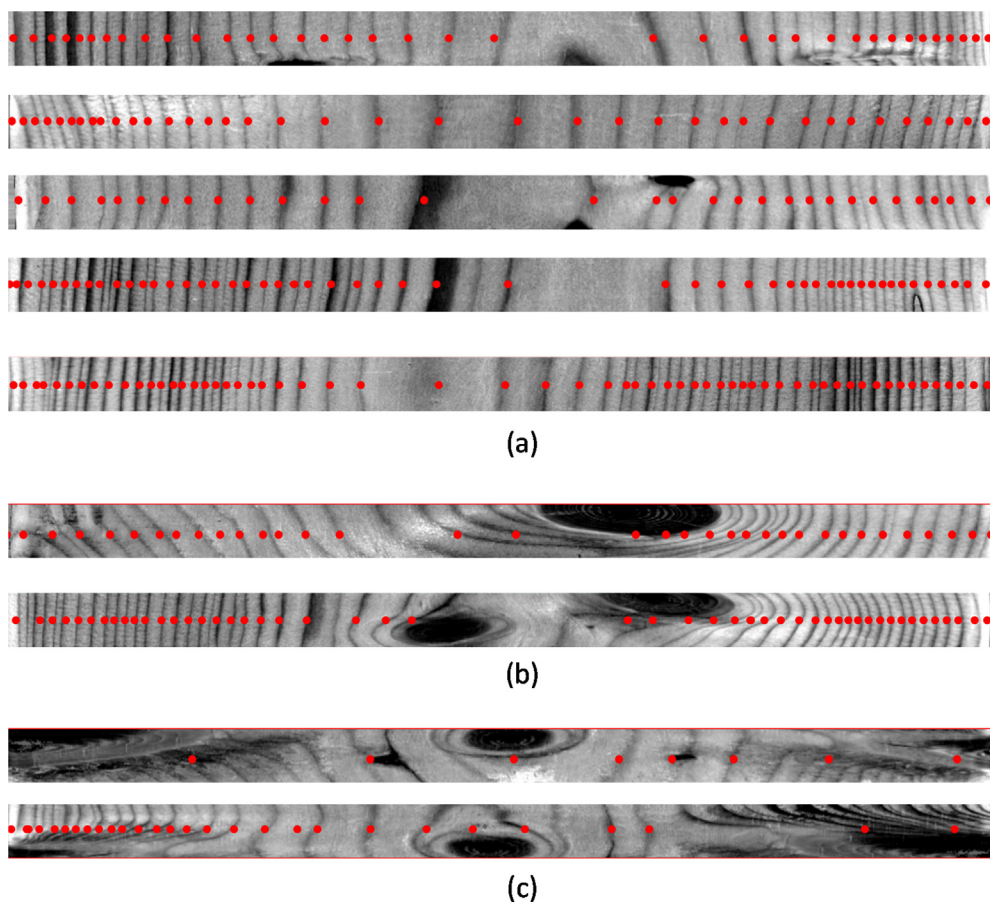


**Fig. 11.** Performance of the surface ring detection method. (a) Examples from clear wood surfaces. (b) Examples of successful detection on knotty surfaces. (c) Examples of inaccurate detection on knotty surfaces.

age ring width per cross-section. The evaluated CT cross-sections included both clear wood and knotty sections.

In the manually estimated profiles, the number of detected rings was obtained by counting the detectable annual rings (i.e., the rings that intersect with at least one wide surface as shown

in Fig. 12). The ring widths were calculated as the difference in radius between each two consecutive rings. In the automatic estimation, the number of detected rings and the average ring widths were calculated at the 300 locations. A moving average filter was then applied on both estimates along the board to reduce the dis-

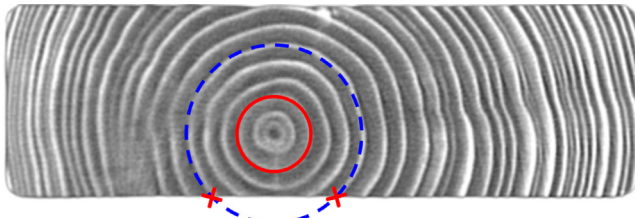


**Fig. 12.** Detectable (dashed blue) vs undetectable (solid red) annual rings. (For interpretation of the references to colour in this figure legend, the reader is referred to the web version of this article.)

turbances around the knots. After that, the number of rings and average ring width at the locations of the 20 manually estimated cross-sections were picked from the filtered estimates.

Four levels of  $\alpha$ , see Eq. (7), namely (0.25, 0.50, 0.75, and 1.00) were attempted in an effort to obtain an appropriate value for this parameter. The mean, median, standard deviations, and percentiles of the error between the automatically and manually estimated number of rings and average ring width under the four  $\alpha$  levels are shown in Table 1 and Table 2. The errors are also displayed as box plots in Fig. 13. The results revealed that when  $\alpha$  is too small (0.25), the method overestimates the number of rings and underestimates the average ring width. The reason is that a small  $\alpha$  value results in a small threshold  $h$ , allowing the same annual ring to be included more than once in the set of unique rings  $U$ . Conversely, when  $\alpha$  is too large ( $\alpha = 1.00$ ), the algorithm underestimates the number of rings and overestimates the rings widths. A good agreement between the automatic and manual radial profiles was obtained with intermediate  $\alpha$  values ( $\alpha = 0.50$  or  $\alpha = 0.75$ ). The minimum error in terms of both the number and widths of detected rings was achieved with  $\alpha = 0.50$ . Accordingly, and based on extensive visual inspection of the automatically estimated radial profiles,  $\alpha = 0.50$  was adopted.

The performance of the proposed method, with  $\alpha = 0.50$ , is demonstrated in Fig. 14. The agreement between the automatic and manual radial profiles is generally very good at clear wood areas (Fig. 14a). Inconsistent performance can be observed at the knotty areas, ranging from very good (Fig. 14b) to inaccurate (Fig. 14c). Again, this is attributed to the fact that both the 1D-CNN and 1D-UNet were trained using artificially generated knot-free surfaces.

#### 4.2. Validation using cross-sections taken at board ends

After a suitable value for  $\alpha$  was found based on the analysis of five CT-scanned boards, the proposed method was validated over the larger and more diverse board set two consisting of 76 boards and hence 152 end cross-sections. Images of all the end cross-sections were labeled using the GUI to obtain a manual estimate of their annual ring profiles. The distribution of the average ring widths, corresponding to the 152 manually estimated ring profiles, is shown in Fig. 15. The manually estimated cross-sectional aver-

**Table 2**

Statistical analysis of the absolute error between the automatically and manually estimated average ring widths in 100 CT-scanned cross-sections.

Quantity	$\alpha = 0.25$	$\alpha = 0.50$	$\alpha = 0.75$	$\alpha = 1.00$
Mean	0.87	<b>0.26</b>	0.42	0.50
Median	0.86	<b>0.25</b>	0.40	0.53
Std.	0.34	<b>0.17</b>	0.28	0.32
85th percentile	1.19	<b>0.44</b>	0.75	0.87
90th percentile	1.27	<b>0.49</b>	0.82	0.94
95th percentile	1.44	<b>0.58</b>	0.88	1.02

age ring widths range from 0.7 to 5 mm with a mean of 2.7 mm and a standard deviation of 0.96 mm.

The automatic procedure described in Section 4.1 to estimate ring profiles at every 20 pixels along the board (approximately 300 cross-sections per board) was also applied on the 76 boards of board set two. The average ring width was computed for each cross-section, and a moving mean filter was then applied over the calculated cross-sectional averages to smooth out the fluctuations near the knots. The automatically estimated average ring widths at the two ends were picked from the filtered ring width estimates.

The results showed a good agreement between the automatic and manual average ring widths with a mean absolute error of 0.322 mm and an  $R^2$  of 0.84. A statistical analysis of the error is given in Table 3. The radial profiles of the vast majority of the cross-sections were accurately estimated. Fig. 16 shows a few examples of automatically estimated cross-sections vs the actual ones.

To identify the limitations of the proposed method, we closely examined the cross-sections with relatively large errors between the automatic and manual estimations. Examples of these cross-sections are shown in Fig. 17. Most of the large errors were found at knotty cross-sections (e.g. Fig. 17a). As discussed earlier, knots affect the performance of both the pith estimator and the surface ring detector resulting in an inaccurate radial profile estimate. Cross-sections with highly irregular annual rings (e.g. Fig. 17b and c) were also problematic since the radial profile estimation algorithm assumes perfectly circular rings. Additionally, the accuracy of the method is limited by various irregularities on boards' surfaces such as surface roughness (Fig. 17d).

In some applications, such as strength grading, the global ring width average over the entire length of a board could be more interesting than individual cross-sectional averages. An automatic estimate of the global ring width average was obtained for each of the 76 boards by calculating the mean of the 300 automatically estimated ring widths. A rough manual estimate of the global ring width average was also calculated for each board by averaging the two ring width means, manually estimated at the two end cross-sections. Table 3 presents a statistical analysis of the error between the automatically and manually estimated global average ring widths. The results indicate that the method was even more successful in estimating the global average ring width per board than in calculating individual averages per cross-section. This is because the local effects of knots and other irregularities are likely to be averaged out when calculating the global average ring width.

#### 4.3. Automatic average ring width as an IP for tensile strength

The automatic ring width estimation method was applied on the 383 Norway spruce boards destructively tested in tension. The cross-sectional average ring widths were estimated at 300 locations per board on average. A moving mean filter was used over the estimated averages to minimize the effects of knots. The automatic global average ring width (AGRW) for each board was

**Table 1**

Statistical analysis of the absolute error between the numbers of automatically and manually detected rings in 100 CT-scanned cross-sections.

Quantity	$\alpha = 0.25$	$\alpha = 0.50$	$\alpha = 0.75$	$\alpha = 1.00$
Mean	15.79	<b>2.65</b>	2.94	3.60
Median	16	3	<b>2</b>	3
Std.	4.68	<b>1.55</b>	2.49	2.58
85th percentile	20	<b>4</b>	6	7
90th percentile	22	<b>4</b>	7	8
95th percentile	25	<b>5</b>	8	8

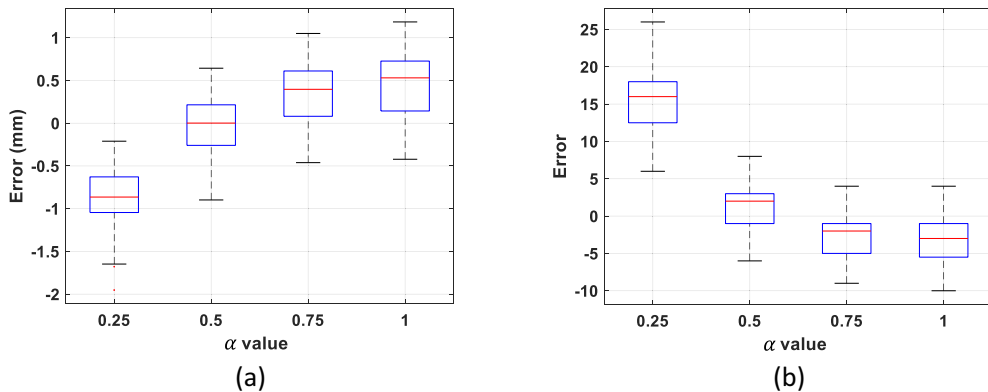


**Fig. 13.** Box plots of the error between automatically and manually estimated annual ring profiles. The error is calculated as the difference between the automatic and manual estimations in terms of: (a) cross-sectional average ring widths, and (b) number of detected rings.

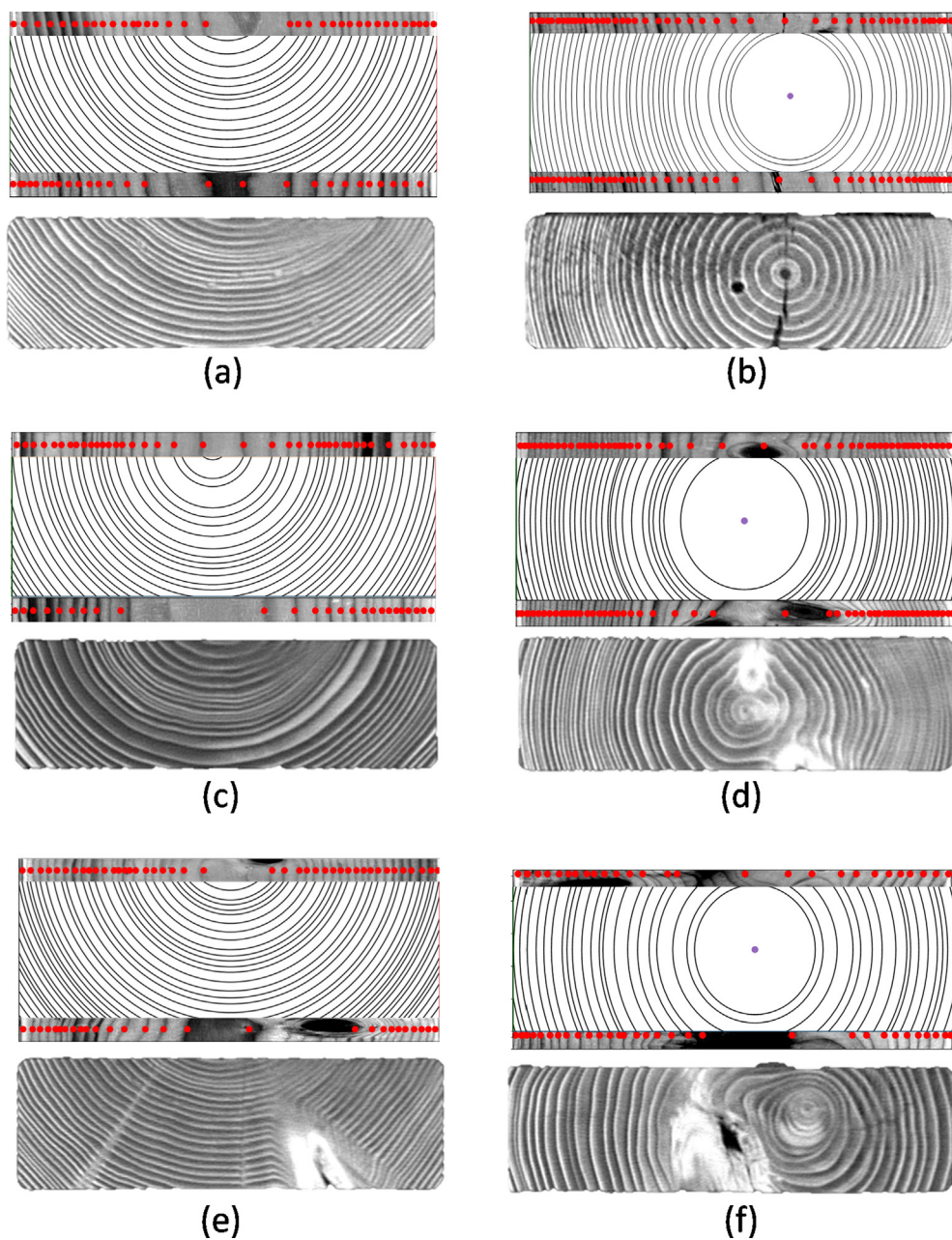


**Fig. 14.** Automatically estimated ring profiles vs actual CT-scanned cross-sections.

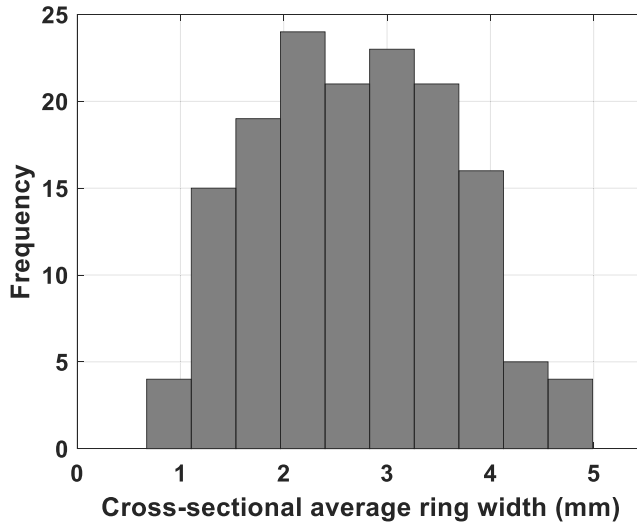


**Fig. 15.** Distribution of the 152 manually estimated cross-sectional average ring widths.

**Table 3**

Statistical analysis of the absolute error (in millimeter, except for  $R^2$ ) between the automatically and manually estimated average ring widths in 76 Norway spruce boards (152 end cross-sections).

Quantity	Per cross-section	Per board
Sample size	152	76
$R^2$	0.84	0.90
Mean	0.32	0.29
Median	0.23	0.21
Std.	0.32	0.24
85th percentile	0.63	0.55
90th percentile	0.72	0.65
95th percentile	0.89	0.79

then calculated as the mean of the filtered cross-sectional averages.

Fig. 18 displays a scatter plot between  $\rho_{cw,12\%}$  and AGRW along with the  $R^2$  and the line of regression. The plot indicates a weak negative correlation between the two variables ( $R^2 = 0.17$ ). These results are in line with the previous studies that investigated the correlation between the density and manually estimated ring width in Norway spruce [9]. Scatter plots between the tensile strength  $f_t$  and individual IPs ( $\rho_{board,12\%}$ ,  $E_{dyn, 12\%}$ ,  $D_{dyn, 12\%}$ ,  $E_{b,90,nom}$ , and AGRW) are presented in Fig. 19. It can be noticed that AGRW correlates better with  $f_t$  ( $R^2 = 0.30$ ) than with  $\rho_{cw,12\%}$ . This level of correlation is consistent with results reported in [8,13] regarding the correlation between  $f_t$  and manually calculated average ring width.

As explained in Section 2.1.3, the sample of 383 boards originated from seven different sawmills and five different sub-regions in Sweden and Finland. In Table 4  $R^2$  between  $\rho_{cw,12\%}$  and AGRW are presented individually for the different regions and it can be noted that when considering one region at a time the relationship is considerably stronger than what it is for the total sample of 383 boards. This indicates that there is a significant relationship between annual ring width and clear wood density but also that there are differences in density between different sub-regions that does not correspond to annual ring width.

Next, different combinations of  $\rho_{board,12\%}$ ,  $E_{dyn, 12\%}$ ,  $D_{dyn, 12\%}$ ,  $E_{b,90,nom}$ , and AGRW were used to formulate nine IPs by means of multiple linear regression. The objective of this investigation was

to evaluate the benefits of incorporating AGRW into the IPs currently used in machine strength grading. The nine IPs investigated are defined as follows:

$$IP_{t,1}(E_{b,90,nom}, \text{AGRW}) = k_{t,0} + k_{t,1} \cdot E_{b,90,nom} + k_{t,2} \cdot \text{AGRW} \quad (13)$$

$$IP_{t,2}(E_{dyn, 12\%}, \text{AGRW}) = k_{t,3} + k_{t,4} \cdot E_{dyn, 12\%} + k_{t,5} \cdot \text{AGRW} \quad (14)$$

$$IP_{t,3}(D_{dyn, 12\%}, \text{AGRW}) = k_{t,6} + k_{t,7} \cdot D_{dyn, 12\%} + k_{t,8} \cdot \text{AGRW} \quad (15)$$

$$IP_{t,4}(E_{dyn, 12\%}, E_{b,90,nom}) = k_{t,9} + k_{t,10} \cdot E_{dyn, 12\%} + k_{t,11} \cdot E_{b,90,nom} \quad (16)$$

$$IP_{t,5}(E_{dyn, 12\%}, E_{b,90,nom}, \text{AGRW}) = k_{t,12} + k_{t,13} \cdot E_{dyn, 12\%} + k_{t,14} \cdot E_{b,90,nom} + k_{t,15} \cdot \text{AGRW} \quad (17)$$

$$IP_{t,6}(D_{dyn, 12\%}, E_{b,90,nom}) = k_{t,16} + k_{t,17} \cdot D_{dyn, 12\%} + k_{t,18} \cdot E_{b,90,nom} \quad (18)$$

$$IP_{t,7}(D_{dyn, 12\%}, E_{b,90,nom}, \text{AGRW}) = k_{t,19} + k_{t,20} \cdot D_{dyn, 12\%} + k_{t,21} \cdot E_{b,90,nom} + k_{t,22} \cdot \text{AGRW} \quad (19)$$

$$IP_{t,8}(\rho_{board,12\%}, E_{b,90,nom}) = k_{t,23} + k_{t,24} \cdot \rho_{board,12\%} + k_{t,25} \cdot E_{b,90,nom} \quad (20)$$

$$IP_{t,9}(\rho_{board,12\%}, E_{b,90,nom}, \text{AGRW}) = k_{t,26} + k_{t,27} \cdot \rho_{board,12\%} + k_{t,28} \cdot E_{b,90,nom} + k_{t,29} \cdot \text{AGRW} \quad (21)$$

where  $k_{t,0}$  to  $k_{t,29}$  are the coefficients of the multiple linear regression, and the subscript  $t$  indicates that the IPs above are used for predicting the tensile strength. The results are summarized in Table 5, which provides the  $R^2$  and SEE values between  $f_t$  and the IP combinations.

The  $R^2$  between  $f_t$  and  $E_{b,90,nom}$  was 0.41. After adding AGRW (i.e.,  $IP_{t,1}$ ), the  $R^2$  increased considerably to 0.52 and the SEE decreased by 0.80 MPa. Interestingly, the  $R^2$  obtained with  $IP_{t,1}$  is significantly higher than the  $R^2$  corresponding to the correlation between  $f_t$  and  $E_{dyn, 12\%}$ . This indicates that calculating AGRW enables commercial laser/optical scanners to predict the tensile strength more accurately than what can be achieved by dynamic excitation alone.

The  $R^2$  obtained when  $E_{dyn, 12\%}$  was used alone to predict  $f_t$  was 0.44. A significant improvement was achieved when adding AGRW to formulate  $IP_{t,2}$  ( $R^2 = 0.53$ ). This indicates that it could be beneficial to use AGRW in addition to  $E_{dyn, 12\%}$  when the scanner available does not have laser scanning capability. In case a laser scanner is available, using  $E_{b,90,nom}$  together with  $E_{dyn, 12\%}$  (i.e.,  $IP_{t,4}$ ) yields better tensile strength predictions. This IP, which is one of the most accurate IPs available today in terms of tensile strength prediction, resulted in a strong correlation ( $R^2 = 0.65$ ). Adding AGRW to this combination (i.e.,  $IP_{t,5}$ ) increased the  $R^2$  slightly to 0.68 and decreased the SEE slightly by 0.30 MPa.  $IP_{t,8}$ , which combines  $E_{b,90,nom}$  with  $\rho_{board,12\%}$ , resulted in an  $R^2$  of 0.61 and SEE = 6.0 MPa. The correlation was slightly improved after adding AGRW to this combination in  $IP_{t,9}$  ( $R^2 = 0.63$ , SEE = 5.8 MPa).

As mentioned earlier,  $D_{dyn, 12\%}$  can replace  $E_{dyn, 12\%}$  in the prediction of  $f_t$  when it is not possible to determine the density. The  $R^2$  between  $f_t$  and  $D_{dyn, 12\%}$  is 0.38, which is lower than the  $R^2$  between

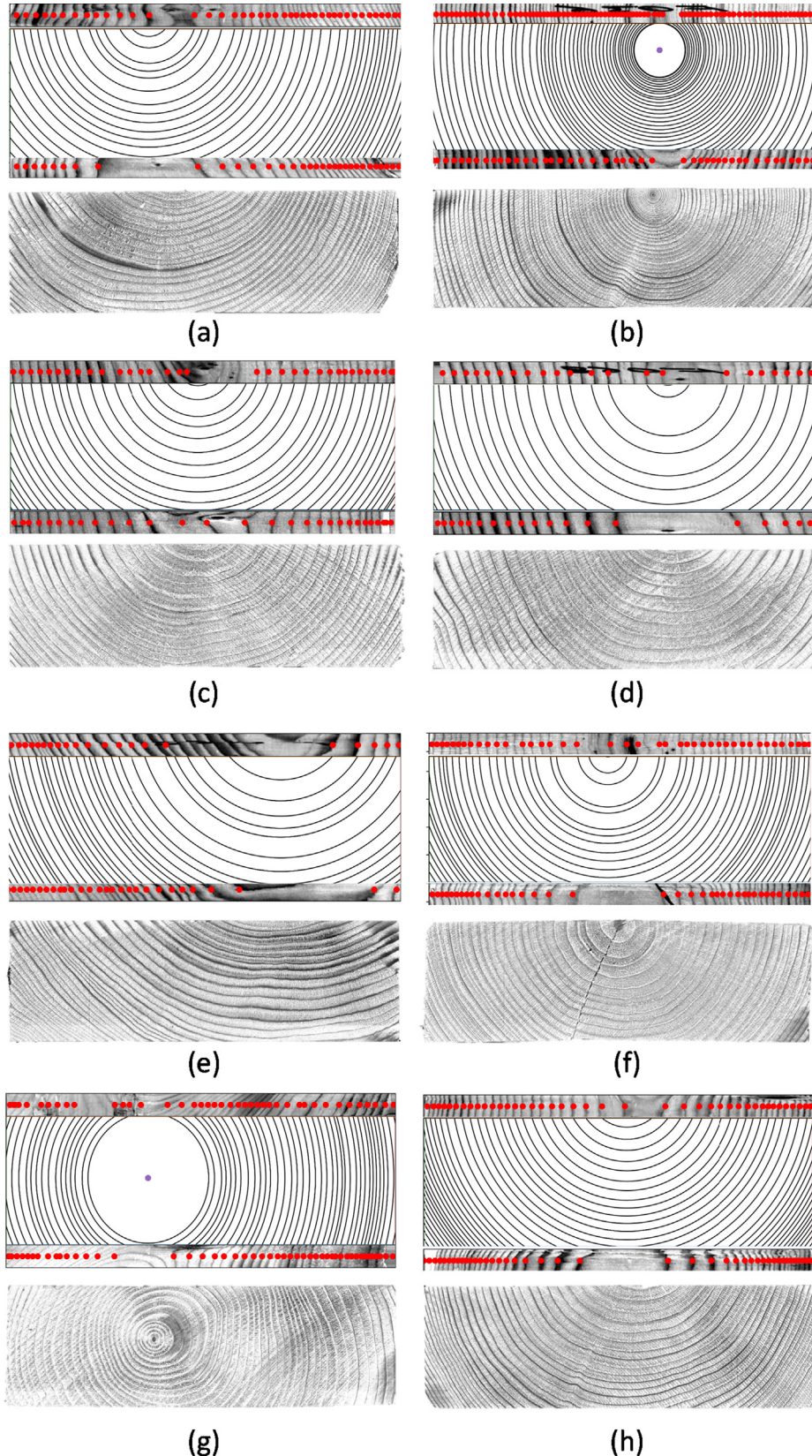


**Fig. 16.** Automatically estimated ring profiles vs actual photographs of clear wood cross-sections.

$f_t$  and  $E_{dyn, 12\%}$  (0.44). However, combining  $D_{dyn, 12\%}$  with AGRW (i.e., IP<sub>t,3</sub>) increased the  $R^2$  considerably to 0.53, which is equal to the  $R^2$  obtained by combining  $E_{dyn, 12\%}$  with AGRW. Moreover, add-

ing AGRW to  $D_{dyn, 12\%}$  and  $E_{b,90,nom}$  in IP<sub>t,7</sub> significantly improved the  $R^2$  compared to when  $D_{dyn, 12\%}$  and  $E_{b,90,nom}$  were used alone in IP<sub>t,6</sub> (0.62 compared to 0.54).

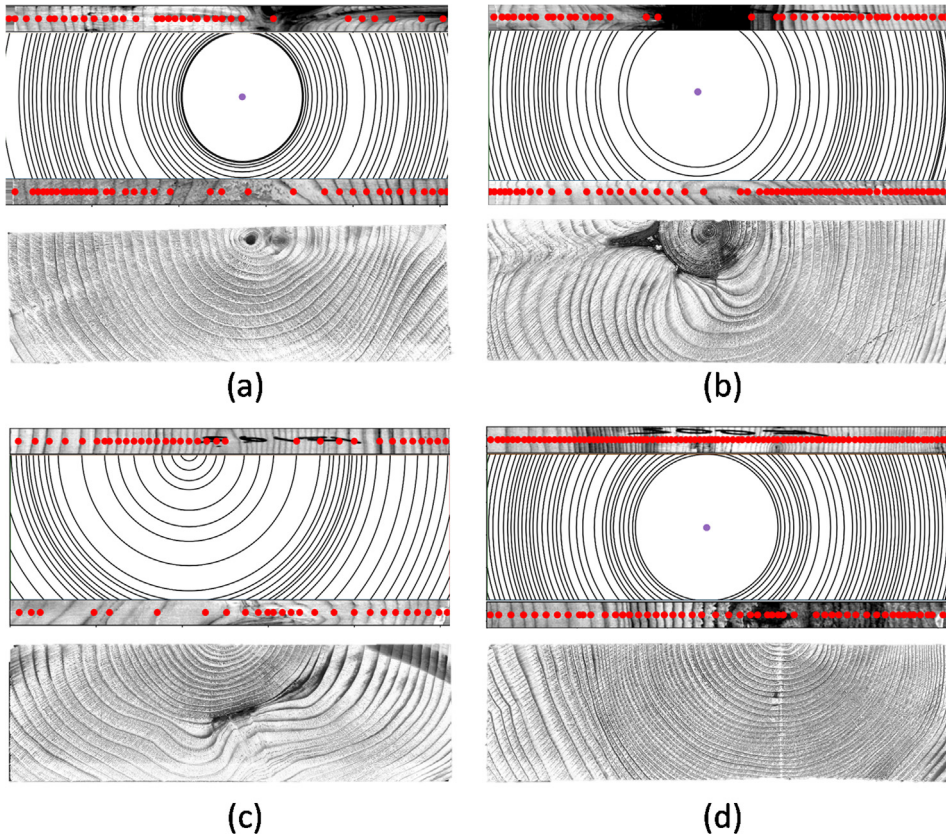


**Fig. 17.** Automatically estimated ring profiles vs actual photographs of knotty and irregular cross-sections.

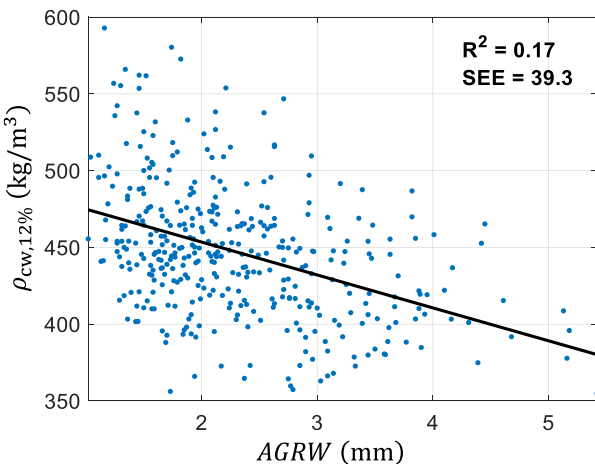


**Fig. 18.** Scatter plot between the  $\rho_{cw,12\%}$  and AGRW for the 383 boards tested in tension.

In summary, it can be concluded that calculating AGRW on the basis of optical scanning can be useful in the following situations:

1. When it is not possible to determine the resonance frequency  $f_1$  or the density  $\rho_{board,12\%}$ , and the only available information are the surface images and fiber orientations obtained by optical and laser scanning.
2. When  $f_1$  is available but determining  $\rho_{board,12\%}$  is not possible.

3. When both  $f_1$  and  $\rho_{board,12\%}$  are available but determining  $E_{b,90,nom}$  is not possible (i.e., when the scanner available does not have laser scanning capability).

In Table 6, correlations between the five different individual IPs are presented to provide further explanation and insight regarding the relationships presented above.

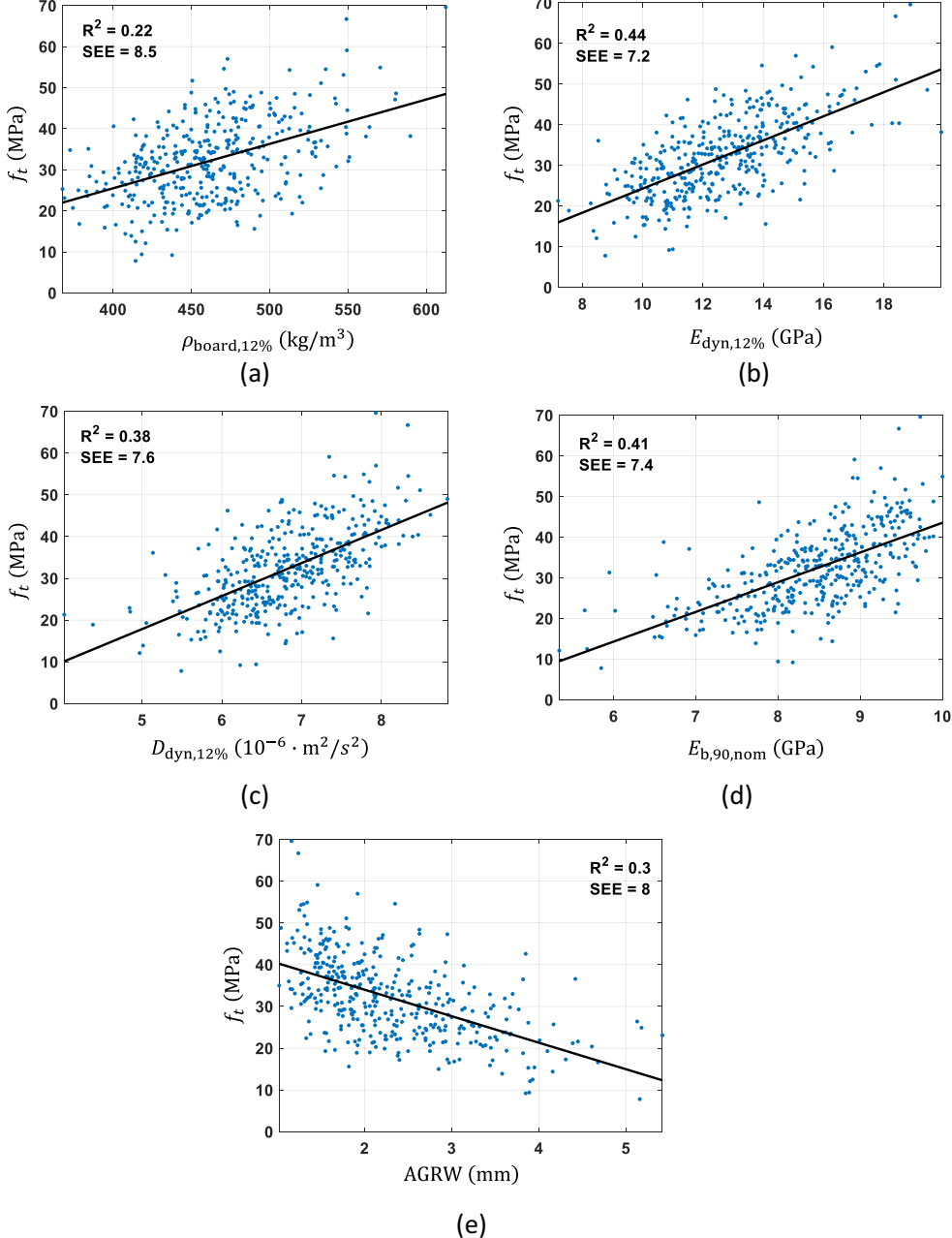
#### 4.4. Automatic average ring width as an IP for bending strength

The corresponding investigation as described in Section 4.3 was conducted on the 409 Norway spruce boards destructively tested in bending. The proposed method was used to calculate AGRW for each board. Again, a weak correlation was observed between  $\rho_{cw,12\%}$  and AGRW as shown in Fig. 20 ( $R^2 = 0.21$ ) for the whole sample, and considerably higher correlations were observed when considering one sub-region at a time, as shown by the results presented in Table 7.

Fig. 21 shows scatter plots between the bending strength  $f_m$  and individual IPs ( $\rho_{board,12\%}$ ,  $E_{dyn, 12\%}$ ,  $D_{dyn, 12\%}$ ,  $E_{b,90,nom}$ , and AGRW). A slightly stronger correlation was obtained between  $f_m$  and AGRW with an  $R^2$  of 0.28. These results are in agreement with the findings reported in [2,8–12] concerning the correlations between  $f_m$ ,  $\rho_{board,12\%}$ , and manually estimated average ring width.

Nine IP combinations were then investigated in order to evaluate the benefits of calculating AGRW in different situations. These IPs can be written as:

$$IP_{b,1}(E_{b,90,nom}, \text{AGRW}) = k_{b,0} + k_{b,1} \cdot E_{b,90,nom} + k_{b,2} \cdot \text{AGRW} \quad (22)$$

Fig. 19. Scatter plots between  $f_t$  and individual IPs.**Table 4**

Coefficients of determination between  $\rho_{cw,12\%}$  and AGRW for sub-sets of boards from different origins and for the total set of 383 boards.

Origin of boards	Number of boards	$R^2$
south-east Sweden	110	0.25
south-west Sweden	48	0.46
mid Sweden	60	0.23
north Sweden	79	0.22
south-east Finland	86	0.32
whole sample	383	0.17

$$\text{IP}_{b,4}(E_{dyn,12\%}, E_{b,90,nom}) = k_{b,9} + k_{b,10} \cdot E_{dyn,12\%} + k_{b,11} \cdot E_{b,90,nom} \quad (25)$$

$$\begin{aligned} \text{IP}_{b,5}(E_{dyn,12\%}, E_{b,90,nom}, \text{AGRW}) = & k_{b,12} + k_{b,13} \cdot E_{dyn,12\%} \\ & + k_{b,14} \cdot E_{b,90,nom} + k_{b,15} \cdot \text{AGRW} \end{aligned} \quad (26)$$

$$\begin{aligned} \text{IP}_{b,6}(D_{dyn,12\%}, E_{b,90,nom}) = & k_{b,16} + k_{b,17} \cdot D_{dyn,12\%} + k_{b,18} \cdot E_{b,90,nom} \\ & + k_{b,19} + k_{b,20} \cdot D_{dyn,12\%} + k_{b,21} \cdot E_{b,90,nom} + k_{b,22} \cdot \text{AGRW} \end{aligned} \quad (27)$$

$$\begin{aligned} \text{IP}_{b,7}(D_{dyn,12\%}, E_{b,90,nom}, \text{AGRW}) = & k_{b,19} + k_{b,20} \cdot D_{dyn,12\%} + k_{b,21} \cdot E_{b,90,nom} + k_{b,22} \cdot \text{AGRW} \end{aligned} \quad (28)$$

$$\text{IP}_{b,2}(E_{dyn,12\%}, \text{AGRW}) = k_{b,3} + k_{b,4} \cdot E_{dyn,12\%} + k_{b,5} \cdot \text{AGRW} \quad (23)$$

$$\text{IP}_{b,3}(D_{dyn,12\%}, \text{AGRW}) = k_{b,6} + k_{b,7} \cdot D_{dyn,12\%} + k_{b,8} \cdot \text{AGRW} \quad (24)$$

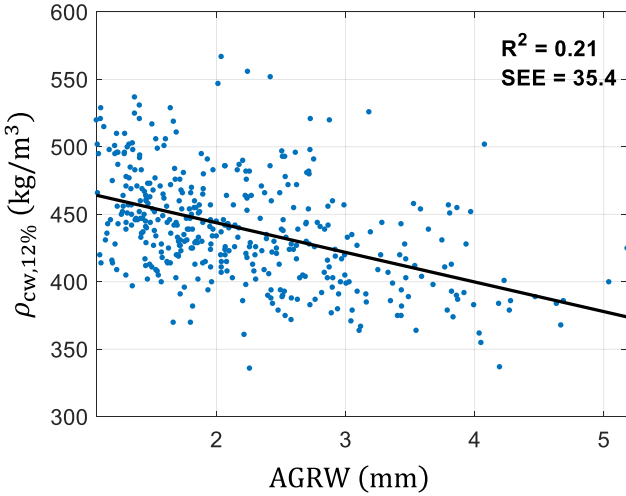


**Fig. 20.** Scatter plot between the  $\rho_{cw,12\%}$  and AGRW for the 408 boards tested in bending.

**Table 5**

Correlation between  $f_t$  and individual and combined IPs. Note that the regression coefficients given in the table correspond to the units shown in Fig. 19.

IP	Correlation with $f_t$	
	$R^2$	SEE
$\rho_{board,12\%}$	0.22	8.5
$E_{dyn, 12\%}$	0.44	7.2
$D_{dyn, 12\%}$	0.38	7.6
$E_{b,90,nom}$	0.41	7.4
AGRW	0.30	8.0
$IP_{t,1} = -6.7 + 5.74E_{b,90,nom} - 4.16 \text{AGRW}$	0.52	6.6
$IP_{t,2} = 11.4 + 2.34E_{dyn, 12\%} - 3.84 \text{AGRW}$	0.53	6.6
$IP_{t,3} = -0.573 + 6.39D_{dyn, 12\%} - 4.69 \text{AGRW}$	0.53	6.6
$IP_{t,4} = -43.2 + 2.30E_{dyn, 12\%} + 5.48E_{b,90,nom}$	0.65	5.7
$IP_{t,5} = -28.5 + 1.99E_{dyn, 12\%} + 4.83E_{b,90,nom} - 2.37 \text{AGRW}$	0.68	5.4
$IP_{t,6} = -48.2 + 5.33D_{dyn, 12\%} + 5.22E_{b,90,nom}$	0.54	6.5
$IP_{t,7} = -26.6 + 4.72D_{dyn, 12\%} + 4.12E_{b,90,nom} - 3.55 \text{AGRW}$	0.62	5.9
$IP_{t,8} = -75.3 + 0.103\rho_{board,12\%} + 7.12E_{b,90,nom}$	0.61	6.0
$IP_{t,9} = -55.6 + 0.0855\rho_{board,12\%} + 6.32E_{b,90,nom} - 2.18 \text{AGRW}$	0.63	5.8

**Table 6**

Correlation between the different prediction variables (individual IPs) for the 383 boards of board set 3.

$R^2$	$\rho_{board,12\%}$	$E_{dyn, 12\%}$	$D_{dyn, 12\%}$	$E_{b,90,nom}$	AGRW
$\rho_{board,12\%}$	1.0	0.64	0.15	0.00	0.17
$E_{dyn, 12\%}$	0.64	1.0	0.72	0.09	0.17
$D_{dyn, 12\%}$	0.15	0.72	1.0	0.19	0.08
$E_{b,90,nom}$	0.00	0.09	0.19	1.0	0.14
AGRW	0.17	0.17	0.08	0.14	1.0

$$\text{IP}_{b,8}(\rho_{board,12\%}, E_{b,90,nom}) = k_{b,23} + k_{b,24} \cdot \rho_{board,12\%} + k_{b,25} \cdot E_{b,90,nom} \quad (29)$$

$$\begin{aligned} \text{IP}_{b,9}(\rho_{board,12\%}, E_{b,90,nom}, \text{AGRW}) \\ = k_{b,26} + k_{b,27} \cdot \rho_{board,12\%} + k_{b,28} \cdot E_{b,90,nom} + k_{b,29} \cdot \text{AGRW} \end{aligned} \quad (30)$$

where  $k_{b,0}$  to  $k_{b,29}$  are the coefficients of the multiple linear regression, and the subscript  $b$  indicates that the IPs above are used for predicting the bending strength.

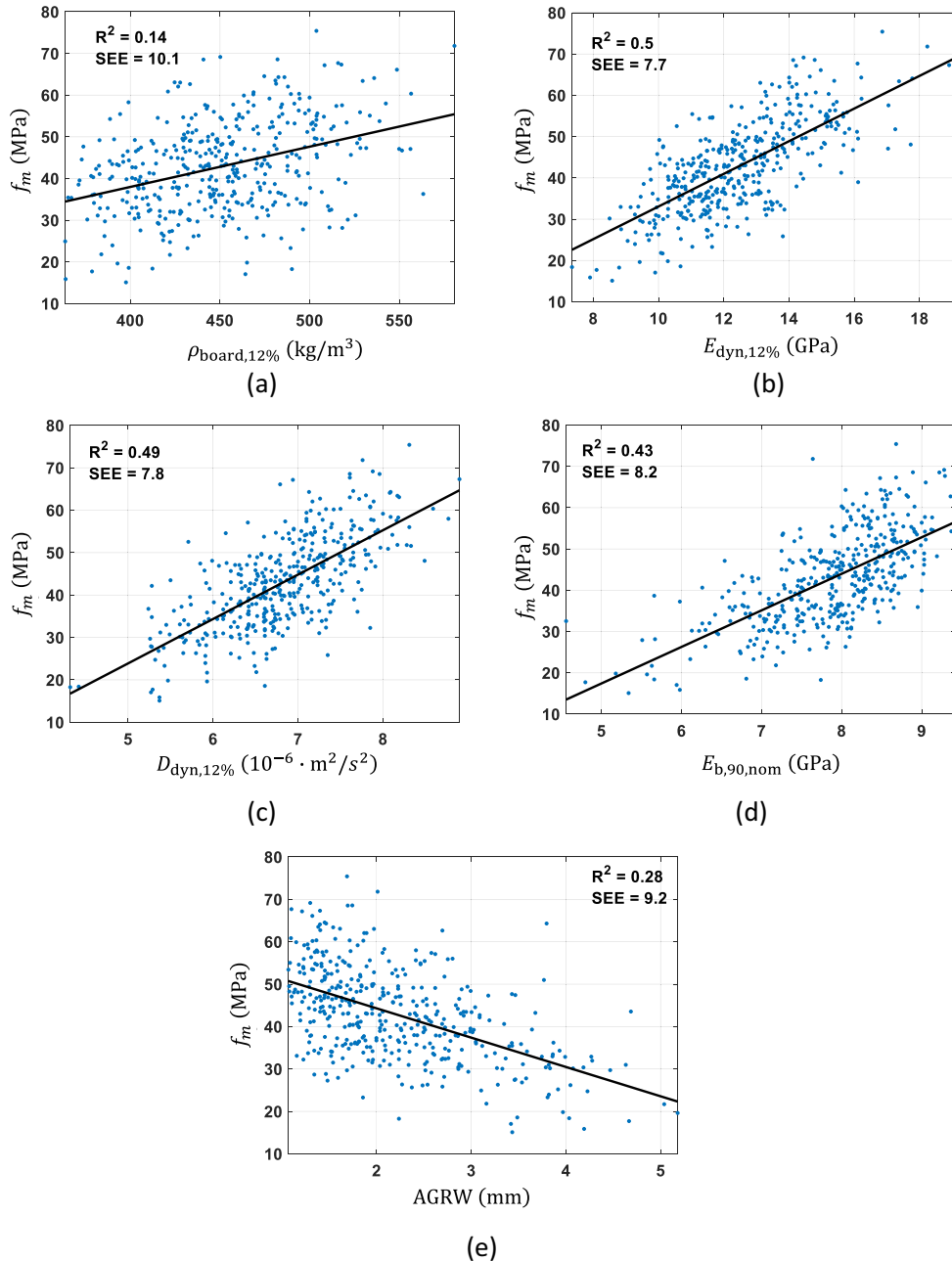
**Table 8** shows the performance of the nine IPs combinations for prediction of bending strength and **Table 9** shows correlations between the five different individual IPs. On an overall level, the potential of using AGRW as an additional predictor variable in definitions of IPs for prediction of bending strength (board set 4) was similar to the potential of using it for prediction of tensile strength (board set 3). However, some interesting differences and similarities of results can be pointed out. First, for board set 4,  $R^2$  between  $E_{dyn, 12\%}$  and  $f_m$  was 0.50 (for board set 3  $R^2$  between  $E_{dyn, 12\%}$  and  $f_t$  was only 0.41) and adding AGRW only increased it to 0.53 (i.e., to the same level as for board sample 3). However,  $R^2$  between  $D_{dyn, 12\%}$  and  $f_m$  was only 0.49 and adding AGRW increased it to 0.55. This means that results from both board set 3 (tension) and board set 4 (bending) indicate that  $D_{dyn, 12\%}$  in combination with AGRW give just as good prediction of strengths as what  $E_{dyn, 12\%}$  in combination with AGRW does. On the other hand, combining  $E_{dyn, 12\%}$  and  $E_{b,90,nom}$  gave better prediction of strength, both for board set 3 and board set 4 ( $R^2$  of 0.65 and 0.69, respectively), than what the combination  $D_{dyn, 12\%}$ ,  $E_{b,90,nom}$  and AGRW did ( $R^2$  of 0.62 and 0.62, respectively, for board set 3 and 4). This may seem contradictory, but can be explained by the following facts. There is no correlation between  $\rho_{board,12\%}$  (which is involved in the definition of  $E_{dyn, 12\%}$ ) and  $E_{b,90,nom}$  but there is a significant correlation between AGRW and the other predictor variables. Therefore, it is particularly effective to combine  $E_{dyn, 12\%}$  and  $E_{b,90,nom}$ . When this is done, adding AGRW does not contribute much further. The correlation between AGRW and  $D_{dyn, 12\%}$  is, however, relatively low and therefore combining  $D_{dyn, 12\%}$  and AGRW gives a considerable improvement compared to using  $D_{dyn, 12\%}$  alone. In conclusion, information of AGRW can in some cases fully compensate for lack of information of density ( $\rho_{board,12\%}$ ) but combined information of density, resonance frequency and fiber orientation is better than combined information of AGRW, resonance frequency and fiber orientation.

Solely based on results from board set 4 and prediction of bending strength, it can be concluded that AGRW could be useful in the following practical situations:

1. When it is not possible to determine  $f_1$  or  $\rho_{board,12\%}$ , and the only available information are the surface images and fiber orientations obtained by optical and laser scanning.
2. When  $f_1$  is available but determining  $\rho_{board,12\%}$  is not possible.

#### 4.5. Computational speed

The method was implemented in Python using a PC with Intel Xeon W – 11955 M CPU at 2.60 GHz (64 GB memory) and an NVIDIA RTX A5000 Laptop GPU. The computational speed of the proposed method was evaluated over the 792 boards tested in tension and bending. The analysis showed that the method requires 383 ms, on average, to determine the pith locations and detect the surface annual rings at around 300 cross-sections per board (1.3 ms per cross-section). The average time required to estimate the corresponding 300 annual ring profiles using the algorithm described in Section 3.4 was 110 ms (0.37 ms per cross-section). The average total time needed to calculate AGRW per board was 493 ms (about 1.7 ms per cross-section). This speed is well above the typical industry requirement of about one second per board, and more than 100 times faster than the method proposed in [23], which required 180 ms per cross-section.

Fig. 21. Scatter plots between  $f_m$  and individual IPs.**Table 7**

Coefficients of determination between  $\rho_{cw,12\%}$  and AGRW for sub-sets of boards from different origins and for the total set of 409 boards.

Origin of boards	Number of boards	$R^2$
south Sweden	32	0.03
south-mid Sweden	78	0.44
mid-north Sweden	60	0.31
north-east Sweden	56	0.41
south Finland	60	0.39
south Norway	63	0.30
south-east Norway	60	0.43
whole sample	409	0.21

**Table 8**

Correlation between  $f_m$  and individual and combined IPs. Note that the regression coefficients given in the table correspond to the units given in Fig. 21.

IP	Correlation with $f_m$	
	$R^2$	SEE
$\rho_{\text{board},12\%}$	0.14	10.1
$E_{\text{dyn. } 12\%}$	0.50	7.7
$D_{\text{dyn. } 12\%}$	0.49	7.8
$E_{\text{b},90,\text{nom}}$	0.43	8.2
AGRW	0.28	9.2
$\text{IP}_{b,1} = -5.1 + 7.10E_{\text{b},90,\text{nom}} - 3.59 \text{AGRW}$	0.50	7.6
$\text{IP}_{b,2} = 7.18 + 3.34E_{\text{dyn. } 12\%} - 2.70 \text{AGRW}$	0.53	7.4
$\text{IP}_{b,3} = -8.19 + 8.68D_{\text{dyn. } 12\%} - 3.68 \text{AGRW}$	0.55	7.3
$\text{IP}_{b,4} = -43.7 + 3.01E_{\text{dyn. } 12\%} + 6.22E_{\text{b},90,\text{nom}}$	0.69	6.1
$\text{IP}_{b,5} = -41.5 + 2.96E_{\text{dyn. } 12\%} + 6.11E_{\text{b},90,\text{nom}} - 0.317 \text{AGRW}$	0.69	6.1
$\text{IP}_{b,6} = -48.8 + 7.25D_{\text{dyn. } 12\%} + 5.36E_{\text{b},90,\text{nom}}$	0.60	6.9
$\text{IP}_{b,7} = -32.8 + 6.62D_{\text{dyn. } 12\%} + 4.53E_{\text{b},90,\text{nom}} - 2.32 \text{AGRW}$	0.62	6.7
$\text{IP}_{b,8} = -70.0 + 0.105\rho_{\text{board},12\%} + 8.47E_{\text{b},90,\text{nom}}$	0.58	7.1
$\text{IP}_{b,9} = -59.6 + 0.0958\rho_{\text{board},12\%} + 7.98E_{\text{b},90,\text{nom}} - 1.107 \text{AGRW}$	0.58	7.0

**Table 9**

Correlation between the different prediction variables (individual IPs) for the 409 boards of board set 4.

$R^2$	$\rho_{\text{board},12\%}$	$E_{\text{dyn. } 12\%}$	$D_{\text{dyn. } 12\%}$	$E_{\text{b},90,\text{nom}}$	AGRW
$\rho_{\text{board},12\%}$	1.0	0.52	0.03	0.00	0.16
$E_{\text{dyn. } 12\%}$	0.52	1.0	0.63	0.13	0.29
$D_{\text{dyn. } 12\%}$	0.03	0.63	1.0	0.29	0.18
$E_{\text{b},90,\text{nom}}$	0.00	0.13	0.29	1.0	0.23
AGRW	0.16	0.29	0.18	0.23	1.0

## 5. Conclusion

This paper proposed a deep learning-based method for estimating annual ring profiles along Norway spruce boards on the basis of optical scanning. The method utilizes a 1D-UNet for detecting surface rings along with a standard 1D convolutional neural network (1D-CNN) to determine the pith location. A radial profile estimation algorithm was developed to determine the radii of the annual rings according to the detected surface rings and the estimated pith location. Both neural networks were trained on a large dataset obtained from thousands of virtual knot-free boards generated by a stochastic log and board generator.

The method was validated on 256 cross-sections obtained from actual Norway spruce boards. The results indicated that all three components of the method (i.e. the pith estimator, the surface ring detector, and the radial profile estimation algorithm) perform very well in clear wood sections. On the other hand, the performance was inconsistent in knotty sections since the two neural networks were trained exclusively on knot-free virtual boards. Both pith location and average ring width estimates exhibited significant disturbances around knots. These disturbances could be mitigated by calculating the pith locations and average ring widths every few millimeters along the board and then applying a moving average filter on both estimates. The coefficient of determination  $R^2$  between the automatically estimated global average ring widths and their manually determined counterparts was 0.895, indicating a very good accuracy. Excluding the knotty sections when calculating the global ring width average may further improve the accuracy. However, this may require adding a fourth component to the method for detecting knots.

The computational speed of the proposed method was more than 100 times faster than the method presented in [23]. Furthermore, the method in [23] only estimates the pith and cross-

sectional average ring width, whereas the proposed method can also identify individual annual rings.

The potential of using the global average ring width AGRW, automatically estimated by the proposed method, as an indicating property in machine strength grading was also evaluated. Two large samples consisting of 383 boards destructively tested in tension and 409 boards destructively tested in bending were used in this investigation. The correlation between AGRW alone and the tensile and bending strengths was not strong. However, combining AGRW with other prediction variables, by means of multiple linear regression, resulted in IPs that could be useful in certain situations. For example, the results demonstrated that AGRW can be used to partially compensate for absence of density and/or axial resonance frequency measurements when predicting the tensile and bending strengths.

In future work, the stochastic board generator can be extended to generate virtual boards with realistic knots. This will allow for training the 1D-CNN and 1D-UNet to better handle knotty areas when estimating the pith location and detecting surface rings without the need for additional filtering or postprocessing.

## Declaration of Competing Interest

The authors declare that they have no known competing financial interests or personal relationships that could have appeared to influence the work reported in this paper.

## Acknowledgement

The authors acknowledge the financial support of the Swedish Knowledge Foundation for funding the research work under grant 20220036-H-01.

## References

- [1] Olsson A, Pot G, Viguier J, Faydi Y, Oscarsson J. Performance of strength grading methods based on fibre orientation and axial resonance frequency applied to Norway spruce (*Picea abies* L.), Douglas fir (*Pseudotsuga menziesii* (Mirb.) Franco) and European oak (*Quercus petraea* (Matt.) Liebl./*Quercus robur* L.). *Annals of Forest Science* 2018;75. <https://doi.org/10.1007/s13595-018-0781-z>.
- [2] Mankowski P, Burawska-Kupniewska I, Krzosek S, Grzeskiewicz M. Influence of pine (*Pinus sylvestris* L.) growth rings width on the strength properties of structural sawn timber. *BioResources* 2020;15:5402–16. , <https://doi.org/10.1537/biores.15.3.5402-5416>.
- [3] British Standards Institution BSI. Bs 4978: Visual strength grading of softwood – Specification; 2011
- [4] . (In Swedish) 2009.
- [5] DIN – Deutsches Institut für Normung. DIN 4074-1: Sortierung von Holz nach der Tragfähigkeit – Teil 1: Nadelholz (Strength grading of wood – Part 1: Coniferous sawn timber). 2012.
- [6] Oscarsson J. Strength grading of structural timber and EWP laminations of Norway spruce - Development potentials and industrial applications. 2014.
- [7] Giaglis K, Timko L, Gryc V, Vavrčík H. Is the quality of the non-native douglas-fir wood produced in the Czech forests comparable to native softwoods? *BioResources* 2019;14:2931–45. , <https://doi.org/10.1537/biores.14.2.2931-2945>.
- [8] Johansson C-J, Brundin J, Gruber R. Stress Grading of Swedish and German Timber: A comparison of machine stress grading and three visual grading systems. 1992.
- [9] Johansson C-J, Boström L, Holmqvist C, Hoffmeyer P, Bräuner L. Laminations of glued laminated timber - Establishment of strength classes for visual strength grades and machine settings for glulam laminations of Nordic origin. 1998.
- [10] Hoffmeyer P. Failure of wood as influenced by moisture and duration of load. 1990.
- [11] Hoffmeyer P. Om konstruktionstræs styrke og styrkesortering (About strength and strength grading of structural timber). *Dansk Skovforening* 1984:34–46.
- [12] Lackner R, Foslie M. Gran fra Vestlandet – Styrke og sortering (Spruce from Western Norway – Strength, stiffness and grading). Report no. 74. n.d.
- [13] Glos P, Heimeshoff B. Möglichkeiten und Grenzen der Festigkeitssortierung von Brettlamellen für den Holzleimbau (Possibilities and limitations regarding strength grading of board laminations for glulam construction). *Ingenieurholzbau in Forschung Und Praxis* (Ehlbeck Und Steck); 1982.
- [14] Olsson A, Oscarsson J. Strength grading on the basis of high resolution laser scanning and dynamic excitation: a full scale investigation of performance. Eur

- J Wood Wood Prod 2017;75:17–31. <https://doi.org/10.1007/s00107-016-1102-6>.
- [15] Bacher M. Comparison of different machine strength grading principles. Proceedings of conference of COST action E53, 29-30 October, Delft, The Netherlands, 2008, 2008, p. 183–93.
- [16] European Committee for Standardization. EN 338:2016: Structural timber – Strength classes. 2016.
- [17] Briggert A, Olsson A, Oscarsson J. Prediction of tensile strength of sawn timber: definitions and performance of indicating properties based on surface laser scanning and dynamic excitation. Materials and Structures/Materiaux et Constructions 2020;53. <https://doi.org/10.1617/s11527-020-01460-5>.
- [18] Longuetaud F, Leban JM, Mothe F, Kerrien E, Berger MO. Automatic detection of pith on CT images of spruce logs. Comput Electron Agric 2004;44:107–19. <https://doi.org/10.1016/j.compag.2004.03.005>.
- [19] Bhandarkar SM, Faust TD, Tang M. CATALOG: A system for detection and rendering of internal log defects using computer tomography. Mach Vis Appl 1998;11:171–90. <https://doi.org/10.1007/s001380050100>.
- [20] J w, d l.. A computer vision method for detection of external log cracks and pith in log cross-section images. In: Proceedings of World Automation Congress: International Symposium on Intelligent Automation and Control (ISIAC). p. 531–6.
- [21] Andreu J, Rinnhofer A. Automatic detection of pith and annual rings on industrial computed tomography log images. Proceedings of ScanTech, 9th International Conference on Scanning Technology and Process Optimization for the Wood Industry, Berkeley, California, Seattle, Washington: 2001, p. 37–47.
- [22] Huber JA, Broman O, Ekevad M, Oja J, Hansson L. A method for generating finite element models of wood boards from X-ray computed tomography scans. Comput Struct 2022;260. <https://doi.org/10.1016/j.compstruc.2021.106702>.
- [23] Habite T, Olsson A, Oscarsson J. Automatic detection of pith location along norway spruce timber boards on the basis of optical scanning. Eur J Wood Wood Prod 2020;78:1061–74. <https://doi.org/10.1007/s00107-020-01558-1>.
- [24] Matthews P, Beech B. Method and apparatus for detecting timber defects. 3976384, n.d.
- [25] Soest J, Matthews P, Wilson B. A simple optical scanner for grain defects. Proceedings of the 5th International Conference on Scanning Technology & Process Control For the Wood Products Industry, 1993.
- [26] Olsson A, Oscarsson J, Serrano E, Källsner B, Johansson M, Enquist B. Prediction of timber bending strength and in-member cross-sectional stiffness variation on the basis of local wood fibre orientation. Eur J Wood Wood Prod 2013;71. <https://doi.org/10.1007/s00107-013-0684-5>.
- [27] European Committee for Standardization. EN 408 (2010) + A1 (2012): Timber structures - Structural timber and glued laminated timber - Determination of some physical and mechanical properties. . n.d.
- [28] European Committee for Standardization. EN 384: 2016: Structural timber – Determination of characteristics values of mechanical properties and density. 2016.
- [29] Habite T, Abdeljaber O, Olsson A. Determination of pith location along Norway spruce timber boards using one dimensional convolutional neural networks trained on virtual timber boards. Constr Build Mater 2022;329:. <https://doi.org/10.1016/j.conbuildmat.2022.127129>.
- [30] Kiranyaz S, Ince T, Gabbouj M. Personalized Monitoring and Advance Warning System for Cardiac Arrhythmias. Sci Rep 2017;7. <https://doi.org/10.1038/s41598-017-09544-z>.
- [31] Zhao R, Yan R, Chen Z, Mao K, Wang P, Gao RX. Deep learning and its applications to machine health monitoring. Mech Syst Sig Process 2019. <https://doi.org/10.1016/j.ymssp.2018.05.050>.
- [32] Salehi H, Burgueño R. Emerging artificial intelligence methods in structural engineering. Eng Struct 2018;171:170–89. <https://doi.org/10.1016/j.engstruct.2018.05.084>.
- [33] Zhang W, Li C, Peng G, Chen Y, Zhang Z. A deep convolutional neural network with new training methods for bearing fault diagnosis under noisy environment and different working load. Mech Syst Sig Process 2018;100:439–53. <https://doi.org/10.1016/j.ymssp.2017.06.022>.
- [34] Ronneberger O, Fischer P, Brox T. U-net: Convolutional networks for biomedical image segmentation. Lecture Notes in Computer Science (Including Subseries Lecture Notes in Artificial Intelligence and Lecture Notes in Bioinformatics) 2015;9351:234–41. [https://doi.org/10.1007/978-3-319-24574-4\\_28](https://doi.org/10.1007/978-3-319-24574-4_28).
- [35] Isola P, Zhu JY, Zhou T, Efros AA. Image-to-image translation with conditional adversarial networks. Proceedings - 30th IEEE Conference on Computer Vision and Pattern Recognition, CVPR 2017 2017;2017-January:5967–76. <https://doi.org/10.1109/CVPR.2017.632>.
- [36] Liu X, Zhou Q, Zhao J, Shen H, Xiong X. Fault diagnosis of rotating machinery under noisy environment conditions based on a 1-D convolutional autoencoder and 1-D convolutional neural network. Sensors (Switzerland) 2019;19. <https://doi.org/10.3390/s19040972>.
- [37] Khessiba S, Blaiech AG, Ben Khalifa K, Ben Abdallah A, Bedoui MH. Innovative deep learning models for EEG-based vigilance detection. Neural Comput Appl 2021;33:6921–37. <https://doi.org/10.1007/s00521-020-05467-5>.
- [38] Ba JL, Adam KDP. A method for stochastic optimization. In: 3rd International Conference on Learning Representations, ICLR 2015 - Conference Track Proceedings. p. 1–15.
- [39] Abadi M, Agarwal A, Paul Barham EB, Chen Z, Citro C, Corrado GS, et al. TensorFlow: Large-scale machine learning on heterogeneous systems. Methods Enzymol 1983;101:582–98.